energies

MDPI

Review

Design of Nanomaterials for Hydrogen Storage †

Luca Pasquini

Department of Physics and Astronomy, Alma Mater Studiorum—Università di Bologna, viale Berti-Pichat 6/2, 40127 Bologna, Italy; luca.pasquini@unibo.it

† Dedicated to Prof. Ennio Bonetti on occasion of his 75th birthday.

Received: 3 June 2020; Accepted: 3 July 2020; Published: 7 July 2020

Abstract: The interaction of hydrogen with solids and the mechanisms of hydride formation experience significant changes in nanomaterials due to a number of structural features. This review aims at illustrating the design principles that have recently inspired the development of new nanomaterials for hydrogen storage. After a general discussion about the influence of nanomaterials' microstructure on their hydrogen sorption properties, several scientific cases and hot topics are illustrated surveying various classes of materials. These include bulk-like nanomaterials processed by mechanochemical routes, thin films and multilayers, nano-objects with composite architectures such as core–shell or composite nanoparticles, and nanoparticles on porous or graphene-like supports. Finally, selected examples of recent in situ studies of metal–hydride transformation mechanisms using microscopy and spectroscopy techniques are highlighted.

Keywords: hydrogen storage; nanomaterial; nanoparticle; thin film; microstructure; interface; elastic strain; transmission electron microscopy

1. Introduction

Hydrogen (H) is recognized across the globe as the ultimate energy carrier with unrivalled potential for sustainable and efficient power applications [1,2]. H has about three times the gravimetric energy density of gasoline (33 kWh/kg against 12 kWh/kg), and its reaction with oxygen in a fuel cell produces clean electricity with only water vapor as an exhaust emission. Intense research is being carried out worldwide on all aspects related to (i) H production from renewable sources [3,4], (ii) fuel cell design, materials, and catalysts [5,6], and (iii) H storage [7–9]. In particular, H storage, the focus of this review, remains a key challenge in the implementation of a H-based energy cycle. In fact, because of the very low critical point (33.2 K) of H_2 gas [10], it is difficult to attain a satisfactory energy content per unit volume. Even at the remarkable pressure of 70 MPa, used currently in the H_2 storage tanks of commercial fuel cell electric vehicles (FCEV), H_2 offers 1.3 kWh/L compared to 8.8 kWh/L of gasoline.

H can be stored in metals that reversibly form a hydride under pressure/temperature conditions suitable for practical applications [7–9,11]. This solution offers the advantage of very high volumetric densities, higher than 70 kg H_2 m^{-3} of liquid H_2, at the expense of a significantly added weight due to the host metal. For instance, the gravimetric and volumetric H densities in MgH_2 are 7.6 wt % H_2 and 109 kg H_2 m^{-3} [12], while the interstitial hydride $TiFeH_2$ attains a maximum 1.9 wt % H_2 [9]; the complex hydride $LiBH_4$ offers the highest gravimetric density of 18.5 wt % available today [13].

However, the gravimetric H capacity does not tell the full story. In fact, in order for a material to become a viable storing option, there are many other requirements to fulfill. One of the most stringent is the temperature T^0, at which H_2 release is possible at standard atmospheric pressure. In order to sustain the endothermic H_2 desorption process using the waste heat from a fuel cell, T^0 must be lower than 100 °C. This figure is beyond the reach of lightweight hydrides such as MgH_2 ($T^0 \approx 286$ °C) and $LiBH_4$, while it is met by the heavier interstitial hydrides like $TiFeH_2$ ($T^0 \approx -8$ °C) [14]. In addition, the material

has to be earth abundant, cost-affordable in terms of synthesis and processing, and environmentally benign. Here below are reported the main key performance indicators set by the US Department of Energy and by the Fuel Cell and Hydrogen Joint Program of the European Energy Research Alliance (EERA) for H storage materials [2,15]:

- Gravimetric H density in the range 5–10 wt % H_2, corresponding to an energy density of 1.6–3.2 kWh/kg.
- Volumetric H density > 50 kg H_2 m^{-3}, corresponding to an energy density > 1.6 kWh/L.
- Thermodynamics: T^0 < 85 °C (transport applications) or < 200 °C (stationary applications).
- Kinetics (tank level): fill time 3–5 min; H_2 release flow 1.6 g/s.
- Durability: 1500 cycles (1/4 tank to full).

Currently, no available material simultaneously satisfies all these requirements. This is the reason, why researchers across the globe are fervently developing advanced H storage materials, both by studying new compounds and by implementing composite architectures, in which different phases are finely dispersed and interact at the nanoscale [11,16]. In this review, I will focus on the design of nanomaterials with significantly improved H storage properties compared to coarse-grained materials with the same chemical composition.

The distinctive feature of nanomaterials is the small extension, in the 1–100 nm range, of their building blocks along one or more directions in space [17]. The number of bulk-sized (i.e., >100 nm) directions defines their dimensionality, which is 0 for nanoparticles (NPs), nanodots, and clusters, 1 for nanowires and nanotubes, and 2 for thin films either as single layers or as stacked multilayers. Whatever their dimensionality, nanomaterials possess a unique charm because they represent a transition walk from the molecular world to the thermodynamic limit, and constitute a family of materials for which surfaces, interfaces, and boundary effects cannot be neglected. Moreover, their nanosize is often comparable to or even smaller than an intrinsic length scale associate with a physical property, such as the electrons' mean free path, leading to so-called confinement effects [18]. These unique properties have stimulated many experimental and theoretical studies of H storage in nanomaterials, aimed at understanding the mechanistic effects of nanosizing and at gaining new tools to tailor the H-metal interaction [16,19–21].

After about twenty years of research, some nanostructure-related effects are well established, such as the enhanced solubility in grain boundaries compared to crystal lattice [22], the influence of interface enthalpy on hydride stability [23,24], and the enhanced sorption kinetics [25,26]. On the other hand, some topics are still in their infancy or even controversial, for instance the strain tuning of desorption enthalpy [27,28], the determination of interfacial entropy, and the existence of a genuine enthalpy–entropy correlation [29,30]. Nanostructuring coupled with dispersion of suitable catalytic additives has proven successful in accelerating H uptake and release [31–33], while the ambition to modify the thermodynamics of H desorption has been harder to fulfill. Recently, significant progresses in transmission electron microscopy (TEM) and spectroscopy techniques have permitted the characterization of single NPs [34–36], shedding light on fundamental aspects of the H-metal interaction and related phase transformations.

Several reviews on the subject of H in nanomaterials are available, which discuss fundamental principles [20,37,38] and/or present a critical analysis of H storage properties [16,39–41]. A comprehensive survey on hydrogen energy materials and technologies, where the interested reader can find up-to-date information on H storage solutions not restricted to nanomaterials, has been published recently [11]. The ambition of this short review is to illustrate the guiding principles adopted for the design of innovative H storage nanomaterials in the last five years, and the materials science concepts behind them. Moreover, selected examples of recent advances in the in situ study of the metal–hydride transformation will be presented, as well.

This review is structured as follows: in Section 2, the thermodynamics and kinetics of hydride formation/decomposition are surveyed first, and then the influence of nanomaterials features on H

storage properties is examined. The subsequent sections focus on specific classes of nanomaterials. Bulk-like nanostructured solids such as those obtained via severe plastic deformation are presented in Section 3, while Section 4 focuses on thin films and multilayers. Nano-objects with composite architectures, like biphasic NPs, are highlighted in Section 5 along with nanoconfined NPs. Finally, Section 6 illustrates in situ structural studies, with emphasis on transmission electron microscopy (TEM) and single particle experiments.

2. Hydrogen in Nanomaterials

2.1. Thermodynamics and Kinetics of Hydride Formation and Decomposition

The thermodynamics of H sorption and hydride formation/decomposition for the case of a simple metal M is illustrated by the pressure-composition isotherms (PCIs) in Figure 1, where the logarithm of the H_2 pressure p_{H_2} is plotted against x_H, the H/M ratio in the solid phase. With increasing p_{H_2}, an increasing amount of H atoms enter as interstitial solutes in the M lattice, following a solvus line that is dictated by the enthalpy and entropy of H solution. The solid solution is usually termed the α phase and is in dynamic equilibrium with the surrounding H_2 atmosphere. Once a limiting composition x_α is attained, the formation of the hydride β phase MH_{x_β} begins according to the reaction:

$$MH_{x_\alpha} + \frac{x_\beta - x_\alpha}{2} H_2 \rightarrow MH_{x_\beta}. \quad (1)$$

The α and β phases coexist until the transformation is completed. In the two-phase field, thermodynamic equilibrium requires the chemical potential of H to be the same in the gas, α, and β phases. In the ideal case this means that the reaction takes place at a constant plateau pressure p_{eq}, given by the van 't Hoff equation:

$$\ln\left(\frac{p_{eq}}{p^0}\right) = \frac{2\Delta g^0}{RT\left(x_\beta - x_\alpha\right)} = \frac{\Delta G^0}{RT} = \frac{\Delta H^0}{RT} - \frac{\Delta S^0}{R}, \quad (2)$$

where p_{eq} is the value of p_{H_2} in equilibrium with α and β phases at temperature T and R is the gas constant; Δg^0 is the Gibbs free energy of reaction (1) at standard pressure p^0, while $\Delta G^0 = \Delta H^0 - T\Delta S^0$ is the same quantity per mole H_2. After complete hydride formation, a further increase of p_{H_2} leads only to a small (if any) additional H absorption and the PCIs become very steep. The reverse path is followed with decreasing H_2 pressure, however H release and hydride decomposition usually start at a plateau pressure lower than for hydride formation, i.e., the system exhibits a certain degree of hysteresis [42,43].

Since ΔH^0 is negative for stable hydrides, Equation (2) implies that the plateau pressure shifts upward with increasing T, as shown in Figure 1. In particular, one can see that the temperature T^0, for which $p_{eq} = p^0$, is given by $T^0 = \Delta H^0/\Delta S^0$. Moreover, in most cases the major contribution to the entropy change ΔS^0 comes from the disappearance of the gas, because the vibrational and configurational entropy of H in the solid are small compared to the entropy of the gas S_{H_2}. Therefore, $\Delta S^0 \approx -S_{H_2} \approx -130$ J/(K·molH_2) (for $p^0 = 1$ bar). These two observations lead to $T^0 \approx -\Delta H^0/130$, explaining why the value of ΔH^0 is so important in determining the technical conditions for H_2 release. In fact, an ideal H storage material should be able to release H_2 close to ambient temperature ($T_0 \approx 300$ K) and pressure, corresponding to an ideal enthalpy value $\Delta H^0 \approx -300 \cdot 130 \approx -39$ kJ/molH_2. Unfortunately, many interesting H storage materials fail to satisfy this thermodynamic requirement. One notable example is MgH_2, amply discussed later on, which is too stable with an enthalpy $\Delta H^0 \approx -74$ kJ/molH_2. As we will see in the next sections, one of the challenges of materials modification by nanostructuring is indeed the shift of the thermodynamics towards more favorable conditions for H_2 release.

The values of ΔH^0 and ΔS^0 are usually determined from the slope and intercept of van 't Hoff plots $\ln\left(p_{H_2}\right)$ vs.T^{-1}, as schematized in the right part of Figure 1. The presence of hysteresis implies

that van 't Hoff plots may be different for H absorption and desorption, yielding slightly different values for ΔH^0 and ΔS^0.

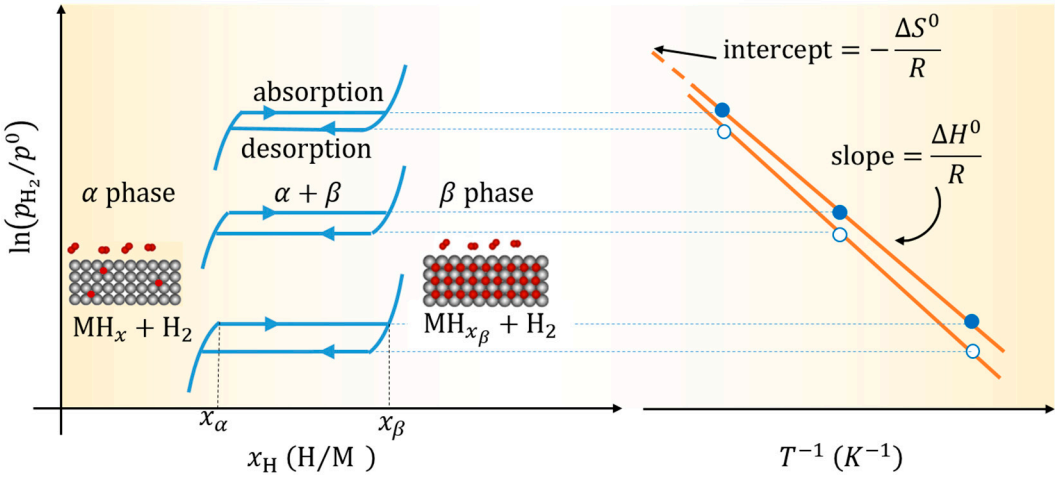

Figure 1. Schematic illustration of the thermodynamics of hydride formation and decomposition. The left part shows pressure-composition isotherms (PCIs) recorded at different temperatures; from the temperature dependence of the plateau pressures for H absorption and desorption, reported in the van 't Hoff plot to the right, the standard enthalpy and entropy of the reaction are determined.

Interstitial metallic hydrides, the prototype and most studied of which is Pd, can be effectively described by the lattice gas model [44]. Here, it is assumed that interstitial sites with energy E_0 can be either empty or occupied by a single H atom up to a maximum composition $r \equiv (\mathrm{H/M})_{max}$. In addition, the H atoms experience a mutual attraction of elastic origin that can be approximated by a H–H pairwise interaction parameter E_{HH}. The chemical potential μ_H of H is then a function of x_H, according to:

$$\mu_H = RT \ln\left(\frac{x_H}{r - x_H}\right) + E_0 - E_{HH} x_H. \quad (3)$$

Turning now to kinetics, there are several elementary processes involved in the overall transformation. Sometimes one of them is the principal rate-limiting step, but the interplay between two or more processes may also dictate the pace. In the case of H absorption, the starting point is the dissociative chemisorption of H_2 at the metal surface. This step is almost barrier-less in Pd, but in general, it involves an activation energy barrier that can be lowered by means of suitable catalysts. Quite often, the surface is contaminated, in particular by oxide species with poor catalytic activity and low permeability to H atoms. If this is so, the material must be activated by exposure to high temperature and H_2 pressure, a potentially harmful procedure for nanomaterials, which are prone to coarsening phenomena. After penetrating in subsurface layers, H diffuses relatively fast in the metal lattice, but the diffusion slows down when the hydride starts to form. For instance, at room temperature the H diffusion coefficient in metallic Mg is $D_H^{Mg} \approx 7{\cdot}10^{-11}$ m^2s^{-1}, but it decreases dramatically to $D_H^{MgH_2} \approx 10^{-18}$ m^2s^{-1} in the hydride material [45]. Therefore, after the formation of an outer hydride layer, H absorption may become rate-limited by H diffusion. The nucleation of the new phase itself is associated with a high elastic strain ε due to the large volume change that accompanies both H absorption and desorption. For instance, the molar volume of MgH_2 is about 32% higher than that of Mg. Therefore, the thermodynamic driving force must be high enough to overcome the strain energy penalty. Furthermore, the nucleation rate decreases exponentially with increasing free energy $\Delta\mathcal{G}_c$ of the critical nucleus, and $\Delta\mathcal{G}_c \propto \gamma^3$, where γ is the specific free energy of the metal/hydride interface. Coherent interfaces are characterized by low γ values and high strain ε, while incoherent interfaces have high γ and low strain ε. The competition between strain energy and interface energy determines what type of interfaces prevail at the various stages of the transformation. As a rule, coherent interfaces are favored for small nuclei because of the

high interface-to-volume ratio, while incoherent interfaces develop when the nuclei grow, in order to release the strain energy that is proportional to their volume. In all cases, pre-existing interfaces such as grain boundaries may act as preferential sites for heterogeneous nucleation, resulting in accelerated nucleation and growth. The motion of the metal–hydride interface requires the thermally activated incorporation or detachment of atoms with local structural rearrangements. If the motion of the interface is the bottleneck of the transformation, one speaks of source-limited or interface-limited case, as opposed to the previously mentioned diffusion-limited scenario. Finally, in the case of H desorption, the last step is the recombination of two H atoms into a H_2 molecule at the surface, which can require a suitable catalyst in a similar way to the dissociative chemisorption that ignites H absorption. Given the complexity of the transformation, it is quite common that the rate-limiting mechanism(s) of H absorption and desorption are different, and so are the apparent activation energies. In order to describe the H sorption kinetics and to gain insight on the atomistic mechanisms behind them, it is custom to calculate the transformed fraction $\alpha(t)$ and to identify the model that best fits its time dependence. Figure 2a illustrates the three most popular models used in the literature to fit experimental H sorption data [46].

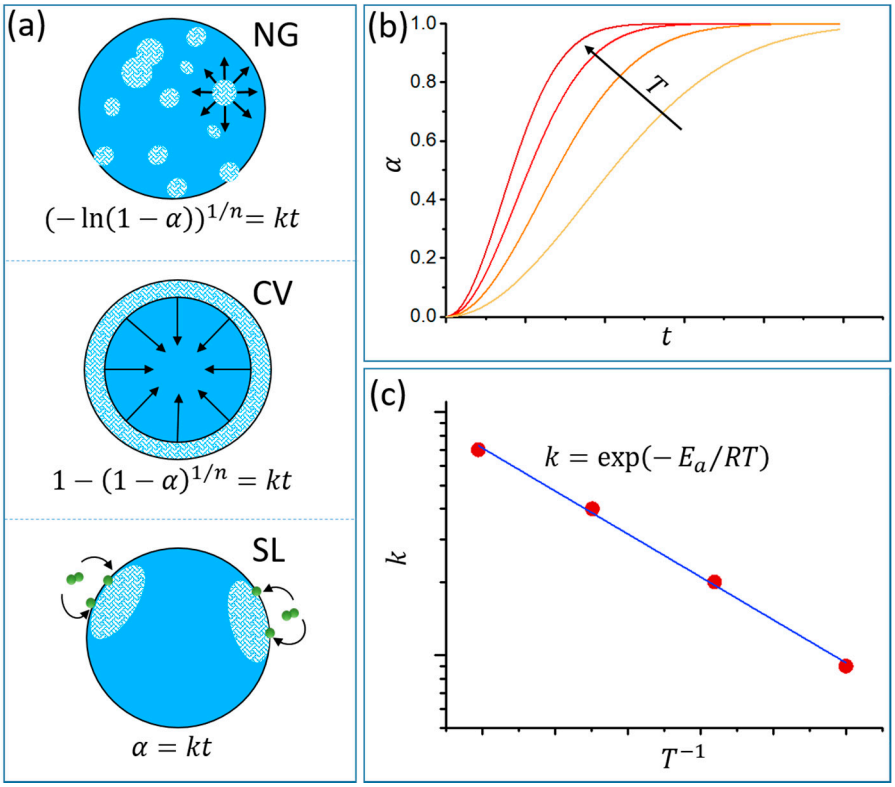

Figure 2. (**a**) Representation of the kinetic models used to analyze the time evolution of the transformed fraction α: nucleation and growth (NG), contracting volume (CV), and surface limited (SL). (**b**) Example of NG kinetics at increasing temperature T. (**c**) Arrhenius plot of the rate constant k, from which the apparent activation energy E_a is determined.

The first model applies to those cases, in which the transformation is rate-limited by nucleation and growth (NG) of the new phase and follows the celebrated Johnson-Mehl-Avrami-Kolmogorov (JMAK) kinetics:

$$\alpha(t) = 1 - \exp\left(-(kt)^n\right), \tag{4}$$

where k is the rate constant and n is known as the Avrami exponent or order of the transformation. It can be shown that $n = a + bc$, where $a = 0$ if all nucleation events occur close to $t = 0$ or $a = 1$ if the nucleation rate is constant in time; intermediate scenarios correspond to $0 < a < 1$. Moreover, $b = 0.5$

or 1 for a diffusion-limited or interface-limited case, respectively, and c is the dimensionality of the growth, e.g., $c = 1$ for 1-D linear growth or $c = 3$ for 3-D spherical growth [46].

As shown in Figure 2a, it is easy to identify a function that is linear in time:

$$\mathcal{F}(\alpha) = (-ln(1-\alpha))^{1/n} = kt. \quad (5)$$

The second model, named contracting volume (CV), describes the situation where the transformed phase forms rapidly as a thin external envelop and then grows progressively until the whole volume is swept. It can also be seen as a special case of instantaneous nucleation that covers the whole surface followed by growth. If the velocity of the moving metal/hydride interface is constant in time, as in interface-limited processes, it is easy to show that:

$$\mathcal{F}(\alpha) = 1 - (1-\alpha)^{1/n} = kt, \quad (6)$$

where k is again the rate constant and n is simply the dimensionality of the growth, i.e., $n = 3$ for a contracting sphere. The functional form for decreasing interface velocity typical of diffusion-limited cases is a bit more complex as discussed in detail by Mintz and Zeiri [46].

The third model, named surface-limited (SL), applies if the rate-limiting step is simply the dissociation or recombination of the H_2 molecule at the surface. If the associated energy barrier does not change with time, for instance because surface catalysts are not affected by the ongoing transformation, the kinetics takes on a particularly simple form:

$$\alpha = kt. \quad (7)$$

Intermediate situations involving for instance the interplay of dissociation and diffusion mechanisms have also been addressed and may well represent the transformation kinetics in certain cases [47]. Since all processes described so far are thermally activated, the kinetics speed up with increasing T, as depicted in Figure 2b. Furthermore, the apparent activation energy E_a can be determined by an Arrhenius plot of $\ln(k)$ vs.T^{-1}, as shown in Figure 2c.

To conclude this section, it is worth to remind that H sorption kinetics depend on the driving force of the transformation, i.e., on the distance between p_{H_2} and p_{eq}. In order to obtain meaningful values of E_a from data measured at different temperatures, it is crucial to select suitable p_{H_2} values so that the driving force is the same in all experiments. This very important point is well described in the works of Rudman [48] and Ron [49], with the latter going deep into the discussion of pressure-dependent kinetics.

2.2. Influence of Nanomaterials Structure on H Sorption Properties

The structural features of nanomaterials, which are responsible for changes of H sorption behavior compared to coarse-grained solids, are schematically summarized in Figure 3. The spotlight is on those features that potentially induce a thermodynamical bias, i.e., a shift $\delta\Delta G^0$ of the free energy (or equivalently, a change $\delta\mu_H$ of the H chemical potential) with respect to coarse-grained counterparts:

$$\delta\Delta G^0 \equiv \Delta G^0_{nano} - \Delta G^0. \quad (8)$$

First, if the external size L_{ext} is small, the change of the specific free energy $\Delta\gamma^{sur} \equiv \gamma^{sur}_{\beta} - \gamma^{sur}_{\alpha}$ that takes place at outer surfaces upon hydride formation may have a non-negligible impact on the overall reaction's free energy. In general, if $\Delta\gamma^{sur} > 0$, the hydride becomes less stable and the plateau pressure at a given temperature increases. The same argument applies to the specific free energy change $\Delta\gamma^{GB}$ at planar defects, e.g., grain boundaries (GBs), and at heterophasic interfaces $\Delta\gamma^{int}$. In both cases, the relative weight depends on some characteristic microstructural length scale L_{mic}. Several types of interfaces can be relevant depending on the system under consideration, for instance matrix/inclusions interfaces in nanocomposites, core/shell interfaces, as well as layer/layer interfaces in

stacked architectures. A correct calculation of the thermodynamical bias must take into account that not only the specific free energy, but also the total area (of surfaces, interfaces, GBs) may change due to volume expansion upon hydride formation. Furthermore, if γ is anisotropic a sum over different crystallographic orientations is necessary [38,50]. However, if the interface area change is small and γ^{int} is isotropic, the bias due to interface free energy can be simplified to [38]:

$$\left(\delta\Delta G^0\right)^{int} = \frac{2\overline{V}_M}{\left(x_\beta - x_\alpha\right)} \frac{A^{int}}{V_{nano}} \Delta\gamma^{int}, \tag{9}$$

where A^{int} and V_{nano} are the total interface area and the volume of the nanoscale object in the α phase; $\overline{V}_M$ is the molar volume of the metal.

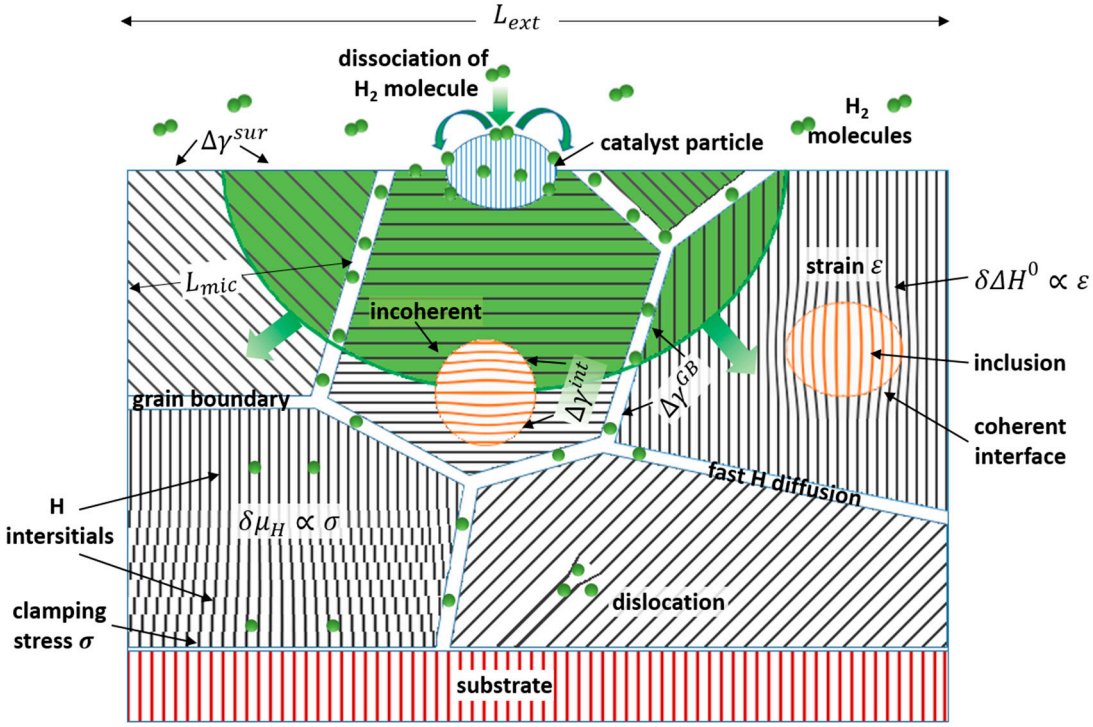

Figure 3. Structural and geometrical features relevant to H sorption in nanomaterials. L_{ext} represents the overall spatial extension of the system, as delimited by either its surface or a supporting substrate. L_{mic} is the characteristic length scale of the microstructure, e.g., its grain size. The growth of the hydride phase, depicted in green, requires H_2 dissociation possibly favored by a catalyst, subsurface penetration, and H diffusion, which is accelerated along internal interfaces or line defects (dislocations). Stress (σ) and strain (ε) fields associated with inclusions or substrate interaction modify the chemical potential μ_H of H or the enthalpy of hydride formation ΔH^0. The specific free energy of interfaces, grain boundaries (GBs) and surfaces undergoes a change $\Delta\gamma$ upon H absorption that leads to a thermodynamical bias. The coherent vs. incoherent nature of the interfaces determines whether long-range strain fields or localized excess free energy bring a relevant contribution to the energetics of the phase transformation.

Another possible source of thermodynamic alteration in nanomaterials are elastic strains ε. For instance, pre-existing tensile strains due to coherent precipitates or to the substrate–film interaction facilitate H insertion in the lattice, making the hydride more stable. The opposite is true for compressive strains. In addition, elastic strains can develop in confined nanomaterials, e.g., core–shell NPs or substrate-clamped films if the system is not free to expand (contract) in response to H absorption (desorption).

The thermodynamic changes induced by elastic strains in Mg-based materials have been studied experimentally and theoretically in thin films [27,51], NPs with core–shell structure [28], and layered nanodots [52]. These models predict an enthalpic destabilization proportional to ε according to:

$$\delta\Delta H^0 = -2B\overline{V}_H\varepsilon, \tag{10}$$

where B is the bulk elastic modulus of the metal, $\overline{V}_H$ is the partial molar volume of H in the hydride, and the strain in the hydride phase ε is negative in compression. As already remarked, the atomic structure of the interfaces, particularly the degree of coherency, is important in assessing the magnitude of strain-related effects.

On the ground of the kinetic models presented in Section 2.1, it becomes clear that the kinetics of H sorption in nanomaterials can be significantly accelerated compared to coarse-grained materials due to the combined effects of several beneficial characteristics, as highlighted in Figure 3. First, a small size L_{ext} implies that H atoms need to diffuse a short distance from the surface to the interior on absorption (and vice versa during desorption). Secondly, the effective H diffusivity along GBs and internal interfaces is orders of magnitude larger than in the bulk crystal lattice. Thirdly, finely dispersed catalyst particles act as effective nanoportals for H_2 dissociation/recombination and subsurface penetration of H atoms. Finally, highly abundant interfaces and surfaces can represent preferential heterogeneous nucleation sites.

The categories of nanomaterials, to which the next sections will pay special attention, are illustrated in Figure 4 and briefly described in the list below:

- Bulk nanocrystalline materials (Figure 4a) have $L_{ext} \gg 100$ nm in all directions and a fine microstructure $L_{mic} \sim 10$ nm. They are prepared by top-down mechanical deformation methods such as severe plastic deformation (SPD) and ball milling.
- Thin films (Figure 4b) are characterized by having $L_{ext} < 100$ nm along one direction, and can be stacked to build multilayers with several heterophasic interfaces. Metal hydride thin films are usually prepared by physical vapor deposition techniques under high vacuum, such as magnetron sputtering or e-beam evaporation, followed by exposure to H_2. The layer–substrate and layer–layer interactions have a measurable impact on the H sorption properties.
- In self-standing nano-objects such as nanoparticles (NPs) and nanowires (NWs; Figure 4c), mutual interactions are negligible and do not influence the metal–hydride transformation. These objects have $L_{ext} < 100$ nm along two (NWs) or three (NPs) directions and can be fabricated both by physical and chemical synthesis techniques.
- Composite architectures, such as supported and embedded nano-objects (Figure 4d), combine several features of the other categories. Most of the time the H-storage units consist in very small NPs (<10 nm). The analysis of H sorption must encompass both the properties of single NPs and their interaction with the surrounding medium.

In order to provide the reader with a quantitative analysis of the benefits brought about by nanostructuring, Table 1 collects the H sorption properties of selected nanomaterials comparing them to those of coarse-grained materials. The focus of Table 1 is on the modification of parameters such as the enthalpy of hydride formation ΔH^0 or the apparent activation energy E_a in a direction favourable to applications. The Mg-H system is the leading actor because a great deal of work has been done to modify its unfavorable thermodynamics and kinetics, in particular to decrease both $\left|\Delta H^0\right|$ and E_a. The Pd-H system has also been widely investigated as a model case, although its H storage capacity is inherently limited by the high mass of Pd and its cost is prohibitive for most applications. The TiFe intermetallic compound has excellent H sorption thermodynamics but suffers from severe activation problems in the bulk, which can be overcome by nanostructuring.

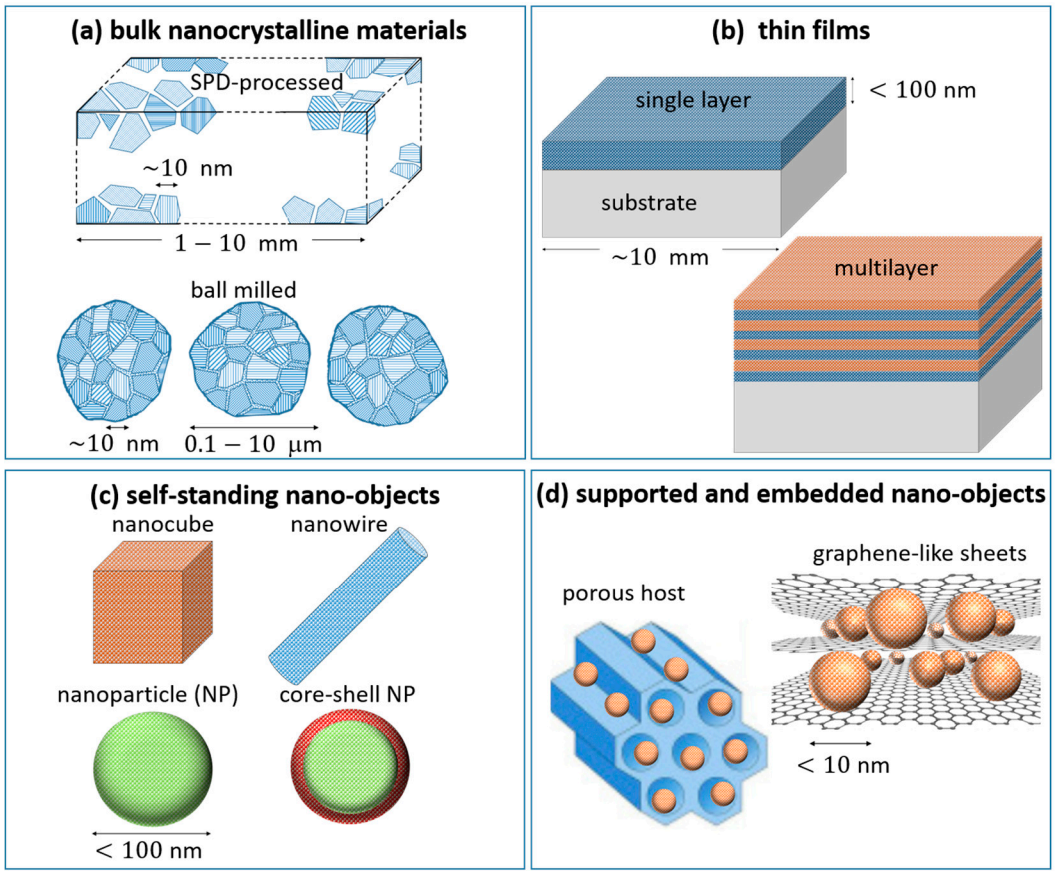

Figure 4. Main categories of nanomaterials for H storage discussed in this review (see text for details).

The selection presented in Table 1 aims at being an orientation guide and is not exhaustive, as the literature on the subject is huge. Many other research works would deserve to be listed. More comprehensive lists can be found for instance in the review by Schneemann et al. [39], who compiled specific tables for NPs, thin films and nanoconfined hydrides, and in the review by Sun et al. dedicated to Mg and its alloys [53].

3. Bulk Nanostructured Materials

The title of this section may sound like an oxymoron. However, it simply means that the external scale $L_{ext} > 100$ nm is large in all three spatial directions, while the microstructure obeys the nanoscale condition $L_{mic} < 100$ nm (see Figure 4).

3.1. Ball Milling

Maybe the most popular processing technique for nanostructured hydrides is ball milling (BM), which produces powders characterized by a typical size of 0.1–10 microns and a nanoscale grain size (Figure 4a). The success of BM is surely due to its versatility, simplicity, and low cost. Apart from powder and grain size refinement, the original application of BM was the preparation of nanostructured alloys, including metastable solid solutions of immiscible elements [54], a reason for which it became known as mechanically alloying. Ball milled MgH_2 with a fine dispersion of additive catalytic phases is one of the best known success stories demonstrating the enhancement of H sorption kinetics [26,55–57], selected examples being listed in Table 1. Moreover, high-energy BM makes it possible to induce gas/solid reactions, in particular hydride formation under H_2 atmosphere [26], as well as solid/solid reactions, for instance the synthesis of mixed-metal complex hydrides [58]. This capability has led to coin the terms mechanochemistry and mechanosynthesis. In some cases, mechanochemistry is the best

procedure to obtain certain complex hydrides [59]. The literature on ball milled H storage materials is impressively vast and in continuous development. The readers who wish to study the subject in deep can consult recent comprehensive reviews [31,59,60].

3.2. Severe Plastic Deformation

Bulk nanostructured materials can also be obtained by methods of severe plastic deformation (SPD) such as high-pressure torsion (HPT) and equal channel angular pressing (ECAP) that form ultra-fine-grained microstructures containing many high-angle GBs [61]. In the HPT process, a sample with the typical shape of a disk is placed between anvils and is subjected at the same time to hydrostatic pressure and torsional straining. SPD techniques can also be applied to the synthesis of binary and ternary alloys, including metastable solid solutions of immiscible elements. The difference between SPD and BM is twofold. First, SPD methods apply a pure shear deformation, while in BM the material undergoes complex deformation processes with possible contaminations from the milling tools. Secondly, the typical size L_{ext} of SPD-processed samples is in the mm to cm range (see Figure 4a), thus offering a higher resistance to ambient atmosphere compared to micrometric powders.

Table 1. H storage properties of selected nanomaterials: gravimetric reversible H storage capacity ρ_m, apparent activation energy E_a of sorption kinetics, and enthalpy ΔH^0 and entropy ΔS^0 of hydride formation/decomposition (in absolute value). L represents the scale of the nanostructure, e.g., grain size, nanoparticles (NPs) diameter, or layer thickness, depending on the system. The data of coarse-grained bulk materials are reported for comparison.

Material	L (nm)	Preparation Method	ρ_m (wt %)	E_a (kJ/mol)	$\lvert\Delta H^0\rvert$ (kJ/molH_2)	$\lvert\Delta S^0\rvert$ (J/K·molH_2)	Ref
bulk Mg	$>10^4$	commercial powders	7	95–130 [a] 120–160 [b]	74	133	[62,63]
Mg NPs	25–38	Cp_2Mg reduction with potassium	~6	115–122 [a] 126–160 [b]			[64]
Mg NWs	30–50	vapor transport	6.8	33.5 [a] 38.8 [b]	65.3 [b]		[65]
Mg-Ti NPs	20	gas phase condensation of Mg-Ti vapors	4.8	52 [a] 35 [b]	67 [c]	119 [c]	[24,33]
Mg-rGO [§] composite	3–4	co-reduction of Mg^{2+} and GO by $C_{10}H_7Li$	6.5	61 [a] 93 [b]			[66]
Ni-doped Mg NPs	6.5	$MgBu_2$ Hydrogenation on graphene	5.4	22.7 [a] 64.7 [b]	62.1 [a]		[67]
Mg	3.4	infiltration of $MgBu_2$ in Ni-doped 3-D carbon	6.6	31 [a] 43 [b]	46.9 [a] 49.1 [b]		[68]
Mg/Cr multilayers	18	magnetron sputtering	6.1	65.7 [b]	73.6 [b]	134 [b]	[69]
Mg-TiH_2	5–10	ball milling (BM)	6.1	58.4 [b]	68.2 [b]	127 [b]	[57]
Mg-Nb_2O_5	~20	BM	6.5	62 [b]			[56]
Ti-coated Mg	~50	BM followed by reaction with$TiCl_3$	6.3	30.8 [b]	75.2 [b]	136 [b]	[70]
Mg-Ni-Y LPSO alloy	5–10	induction melting + pulverization + BM	5.8				[71]
bulk Pd	$>10^4$	black Pd	0.6		36.4 [a]	90 [a]	[72]
Pd NPs	2.6	solution chemistry/PVP	~0.4		31 [a]	67 [a]	[72]
Pd NPs	7.0	solution chemistry/PVP	~0.4		35 [a]	83 [a]	[72]
Pd cube	14	solution chemistry/CTAB		18 [a] 47 [b]	27 [a]	61 [a]	[73]
Pd cube	18	solution chemistry			32 [a]	78 [a]	[35]
bulk TiFe	$>10^4$	precursors melting	1.9	activation issues	28.1 [b]	106 [b]	[14]
TiFe	~10	high pressure torsion	1.7	reversible H-sorption at RT without activation			[74]

[a] Value obtained from H absorption measurements. [b] Value obtained from H desorption measurements. [c] Value calculated from the average of absorption and desorption measurements. [§] Reduced graphene oxide.

BM and SPD can also be combined by applying HPT to ball milled powders, which results in a nanostructured bulk sample with very little porosity and ultra-fine microstructure [75]. The typical microstructure produced by SPD, characterized by small crystallites and a high density of lattice defects (GBs and dislocations), is well illustrated by TEM images of a HPT-processed Ti-V alloy in Figure 5a–d [76].

Several investigators have applied SPD methods both to synthesize new materials and to improve the H storage properties of various alloys and intermetallic compounds, mostly in Mg-based and Ti-based systems [76–81]. The beneficial effects induced by the peculiar microstructure of HPT-processed materials on their H sorption kinetics have been reviewed recently [82].

One remarkable result is the overcoming of the activation problem and the increased air resistance of TiFe alloys [83], which normally require high pressure and temperature to activate the first H absorption and are prone to quick passivation when exposed to air. The activation mechanism, illustrated in Figure 5e, exploits the fact that atomic diffusion is enhanced after HPT and becomes relevant even at room temperature. This is due to the high density of crystalline defects such as vacancies, dislocations, and GBs. The accelerated diffusion promotes surface segregation leading to the growth of Fe-rich islands (depicted in blue in Figure 5e) that are able to catalyze H_2 dissociation. Moreover, the high number of GBs and cracks introduced by HPT facilitates the transport of atomic H from the surface to the inner regions [83]. The resistance to long-time storage in air indicates that GBs are fast pathways for H diffusion and not for oxygen that would deactivate the material. In addition to grain refinement, also the formation of defected amorphous regions is effective in accelerating H transport within the material.

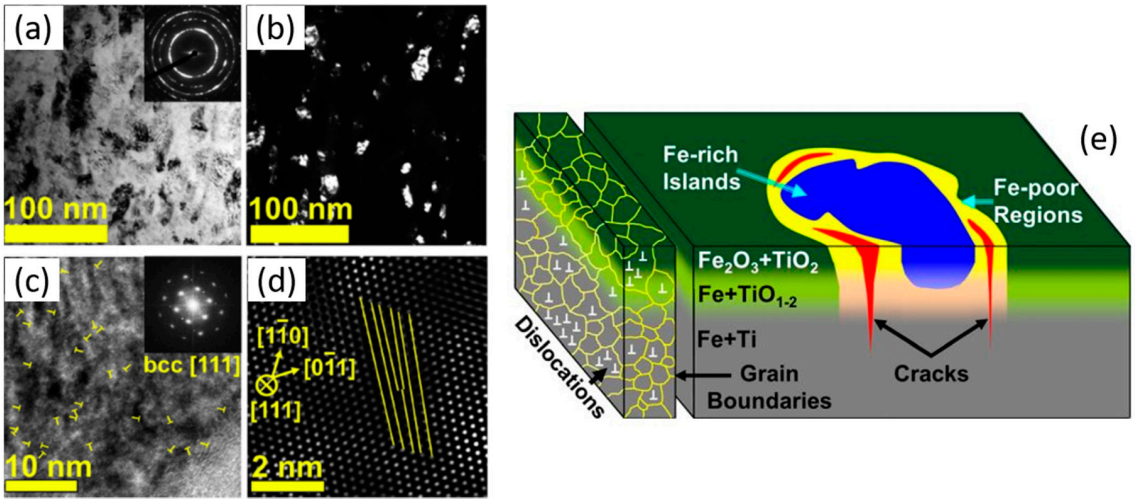

Figure 5. (**a**–**d**) Microstructure of a Ti-V alloy after 100 high-pressure torsion (HPT) turns. (**a**) Bright field TEM image with selected area electron diffraction. (**b**) Dark field TEM image. (**c**) High resolution TEM image and corresponding fast Fourier transform (FFT); edge dislocations are indicated by yellow T. (**d**) Atomic resolution image of an edge dislocation. Reprinted with permissions from [76] (copyright 2016 Elsevier). (**e**) Schematic illustration of the activation mechanism of TiFe by HPT (see text for detailed explanation). Reprinted with permissions from [83] (copyright: 2013 AIP Publishing).

Additional lattice defects induced by SPD, such as dislocations and stacking faults (see Figure 5c,d), had a significant impact on H storage. Stacking faults coupled with partial dislocations constitute fast diffusion paths for H similar to GBs. Mg_2Ni with a high density of stacking faults produced by HPT can absorb 2 wt % H within few minutes at 423 K while a coarse-grained material requires about 20 h to absorb a similar amount [81]. Dislocations generated during HPT have been suggested to play a role in increasing the H storage capacity of a Mg-Ni alloy [78].

The HPT method has been also employed to synthesize new Mg-based and Ti-based alloys and compounds by exploiting solid-state phase transformations. In the case of Mg-based materials,

nanocrystalline intermetallics are obtained in all systems that have stable intermetallic phases. Moreover, amorphous phases form in Mg-Al and Mg-Zn alloys, while metastable bcc, fcc, and hcp phases are observed in the immiscible binary systems Mg-Ti and Mg-Zr [82]. Besides binary alloys, new ternary Mg-based systems such as bcc Mg_2VNi and amorphous Mg_4NiSn have been successfully synthesized by HPT. The number of HPT turns for the synthesis has to be in the range n = 100–1000, well above the typical n = 1–10 turns needed for crystallite size reduction or to achieve maximum hardness [82].

3.3. Long-Period Stacking Ordered Structures

An emerging group of Mg-based ternary alloys, such as Mg-Y-Zn and Mg-Gd-Al, contain a series of novel structures named long-period stacking ordered (LPSO) structures that have raised significant interest because they confer superior mechanical properties and their formation mechanism is intriguing [84]. The LPSO structure was originally discovered in a nanocrystalline bulk alloy $Mg_{97}Zn_1Y_2$ prepared by warm extrusion of rapidly solidified powders [85]: it exhibits both long-period chemical-order and stacking-order. Periodic modulations of the concentration of Zn and Y are observed along the *c* axis of hcp Mg, while the most common stacking orders are of type 18R and 14H [86].

Within this class of alloys, Mg-Ni-Y alloys have gained attention thanks to the good H storage properties, in terms of both gravimetric capacity (up to 6 wt %) and sorption kinetics [71]. The initial structure of the alloy is shown by the TEM micrographs in Figure 6a,b. Domains of the LPSO phase with stacking order of type 18R are present within the Mg matrix. The mechanism, by which the LPSO phase enhances the sorption kinetics of the alloy, has been investigated by x-ray diffraction and TEM [71,87]. These studies reveal that during the first hydrogenation reaction, the LPSO phase decomposes into highly dispersed nanocrystals of MgH_2 + Mg_2NiH_4 + YH_x, as schematized in Figure 6c. The resulting fine microstructure facilitates H diffusion along interfaces and nucleation of the new phase at the GBs. It must be noted that the first H absorption modifies irreversibly the microstructure of the alloy: in fact, the LPSO is not recovered upon H desorption, which eventually leads to Mg, Mg_2Ni, and YH_2 (Figure 6c).

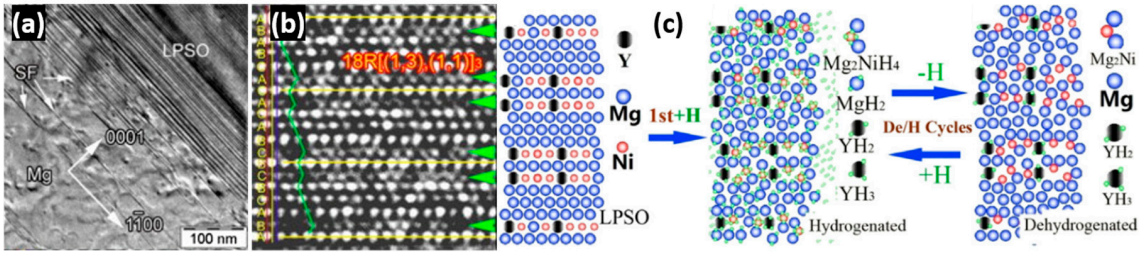

Figure 6. Original microstructure and H-induced local composition changes in a Mg-Ni-Y alloy that contains the 18R-LPSO phase. (**a**) Bright field TEM image showing the 18R-LPSO phase in proximity to Mg; stacking faults (SF) in Mg are indicated by arrows. (**b**) High resolution TEM of the 18R-LPSO phase; the staking sequence of close-packed planes is indexed. (**c**) The LPSO structure is irreversibly lost during the first H absorption, which leads to a fine dispersion of MgH_2, Mg_2NiH_x, and YH_x nanocrystallites (see text for detailed explanation). Reprinted with permissions from [71] (copyright 2013 Elsevier).

According to these experiments, Mg-based alloys with a LPSO phase can be seen as good precursors for H storage materials with finely dispersed phases that boost H-sorption kinetics.

Quite recently, the genuine effect of the long-period ordering on the H-sorption kinetics has been investigated using Mg-In alloys with different In contents as model systems [88]. The alloys were prepared by ball milling of Mg and In precursors with the addition of amorphous carbon to avoid agglomeration. The authors concluded that Mg-In alloys with the presence of LPSO exhibit a lower activation energy for H desorption, leading to improved kinetics compared to the disordered state.

However, the gain comes at the expenses of a significantly decreased storage capacity due to the high In content in the ordered alloys.

4. Thin Films

Metal hydride thin films and multilayers have invariably proven of utmost utility for unraveling the H interaction with metal surfaces as well as the atomistic mechanisms underlying the metal–hydride transformation. In addition, they have a great technological value for the development of hydrogen sensors and smart devices [89,90]. In the following, I will discuss the effects of elastic strains and interface free energy on their thermodynamics.

4.1. Elastic Strains in Thin Films

Wagner and Pundt have investigated systematically the chemical potential μ_H of H in Pd films as a function of film thickness, grain size, and mechanical stress [91]. They found that the H–H interaction energy E_{HH}, which is responsible for precipitation of the solid solution into hydride domains above the solubility limit, diminishes from the bulk value $E_{HH} \approx 37$ kJ/mol down to 15–20 kJ/mol for a film thickness of 10 nm. Two factors contribute to the observed decrease: the reduction of the in-plane grain size and the decreasing thickness. Both can be traced back to the elastic nature of the H–H attractive interaction in metallic hydrides as described by the lattice gas model. In fact, an interstitial H atom causes an elastic dilatation that renders the lattice more attractive for the insertion of additional H. Therefore, any microstructural or geometrical constraints that limit the spatial range of strain fields induced by H will result in a decreased H–H interaction. The reduction of the film thickness imposes a vertical (out-of-plane) geometrical constraint, while the grain size brings in a lateral (in-plane) microstructural constraint due to the open nature of the GBs that do not transmit the strain field. The microstructural contribution to the lowering of E_{HH} can reach ≈ 8 kJ/mol, as estimated by comparing Pd thin films to a thick nanocrystalline Pd sample with no geometrical constraints [91]. The effect of film-substrate clamping stress σ on the thermodynamics is described by introducing a correction $\delta\mu_H$ to the H chemical potential:

$$\delta\mu_H(\sigma) = -2\overline{V}_H\alpha_H\sigma(x_H), \tag{11}$$

where $x_H \equiv$ H/Pd, $\alpha_H = 0.063$ for Pd is the expansion factor defined by $\Delta a/a = \alpha_H x_H$, a being the lattice parameter, and $\overline{V}_H$ is the partial molar volume of interstitial H. Figure 7, reproduced from [91], depicts schematically σ and μ_H as a function of x_H.

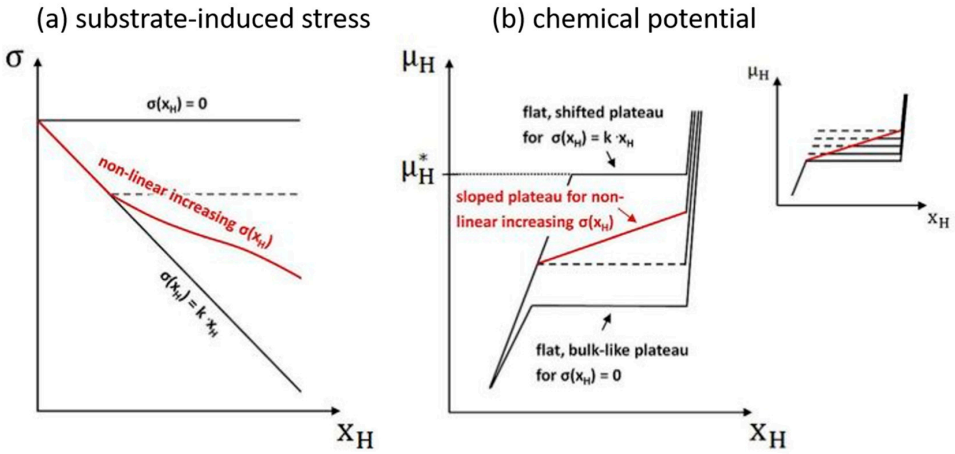

Figure 7. Effects of stress on the thermodynamics of Pd-H thin films. In the presence of substrate-induced stresses linear with concentration, $\sigma = k{\cdot}x_H$, the transformation to hydride takes place at shifted chemical potential μ_H^* compared to bulk Pd. However, if stresses partially relax before μ_H^* is reached, a sloped plateau is observed. Reprinted with permission from [91] (copyright 2016 Elsevier).

If $\sigma(x_H)$ is linear with x_H, the stress shifts upward the equilibrium plateau producing the same effect of a reduced E_{HH} interaction. However, if $\sigma(x_H)$ deviates from linearity because of plastic deformation, due, e.g., to emission of dislocation loops at the hydride/metal interface, the isotherms exhibit a sloping plateau, as if the equilibrium chemical potential increased with x_H. The stress in the film attains the highest values for the thinnest films, where dislocation emission is energetically inhibited and phase coherency is maintained. In this condition, the stress-induced change of the H–H interaction energy amounts to about 3–5 kJ/mol.

The geometrical and microstructural constraints, along with substrate-induced elastic strains, all lead to a destabilization of the hydride through the reduction of the attractive H–H interaction. Therefore, even the critical temperature for hydride formation is reduced compared to the bulk, and shows a dependence on grain size, film thickness, and mechanical stress similar to E_{HH} [91].

The possibility of strain-tuning the desorption enthalpy has attracted significant interest in the case of Mg that suffers from a too high stability [63]. The first experimental suggestion of elastically induced destabilization of MgH_2 was reported in Pd-capped thin films showing an upward shift of the H absorption pressure [27]. This increase was attributed to the clamping of Mg by Pd and interpreted on the basis of Equation (10). However, subsequent experiments pointed out that also Mg-Pd alloying contributes to the pressure increase [92], thus questioning the magnitude of the strain-related effect. Finally, a recent investigation of $Mg_{1-x}Pd_x$ thin films concluded that both clamping and alloying shift the H absorption pressure; however, clamping does not affect the H desorption pressure, and therefore does not induce the desired hydride destabilization [93]. A slight increase of the equilibrium pressure was also reported in Mg/Ti/Pd layered nanodots with decreasing diameter. The strain-related part of this effect was estimated as $\approx$ 1.3 kJ/molH_2, which is significantly smaller than expected for a purely elastic deformation. The main issue against the practical exploitation of mechanical stresses for a strain-controlled thermodynamics seems to be the transition from elastic to plastic behavior. In fact, if high stresses cause plastic deformation, the magnitude of the thermodynamical bias set by Equation (10) is suppressed, while the absorption/desorption hysteresis increases [28,43,52,93,94].

A successful example of strain-induced bias was recently reported for yttrium hydride films that contain immiscible Zr clusters. These inclusions give rise to compressive strains that shift upward both the absorption and the desorption plateau of the $YH_2 \leftrightarrow YH_3$ transformation, demonstrating an effective decrease of hydride stability [95].

4.2. Interface Free Energy in Thin Films

The first pioneering studies of interface-controlled thermodynamics in the Mg-H system made use of Mg-Ti multilayers of various thicknesses [23,96]. As an example, the atomic structure of a Mg(4 nm)/Ti(2 nm) multilayer is illustrated by the TEM micrograph in Figure 8a. TiH_2 is rapidly formed upon exposure to H_2 and does not decompose due to its high stability. Therefore, the system switches back and forth from an MgH_2/TiH_2 multilayer to an Mg/TiH_2 multilayer upon H absorption and desorption. A Pd capping layer on top of the stack facilitates the dissociation and recombination of H_2 and avoids oxidation. Hydrogenography experiments carried out on these multilayers have demonstrated that the thermodynamical bias due to the interface free energy change scales inversely with the thickness of the Mg layer, providing an effective tool to tailor the plateau pressure [23]. From the thickness dependence, it was estimated that $\Delta\gamma^{int} = 0.33$ Jm^{-2} [23] (see Equation (9)). This value is in qualitative agreement with theoretical calculations of the interface energetics carried out for specific orientations of the interface plane, an example of which is shown in Figure 8b [51]. The estimated $\Delta\gamma^{int}$ corresponds to a thermodynamical bias $\delta\Delta G^0 \approx 5$ kJ/molH_2 for the thinnest Mg layer of 2 nm.

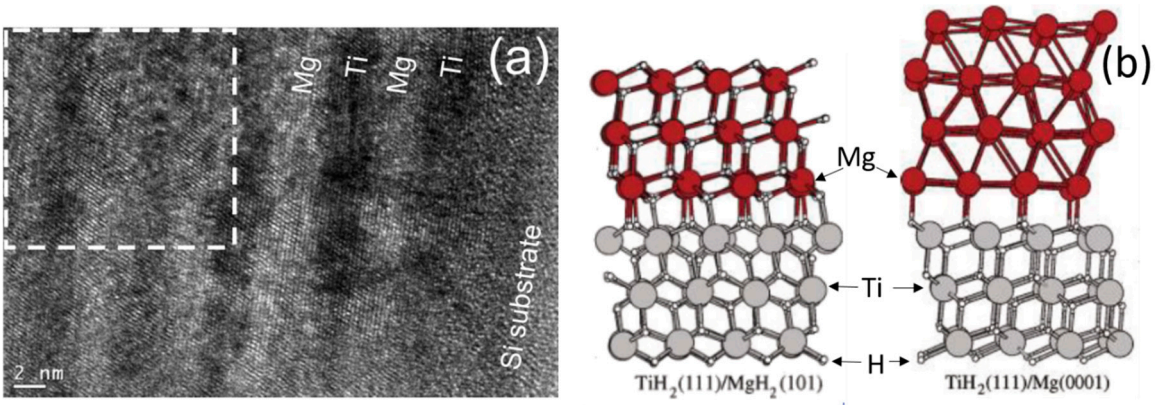

Figure 8. (**a**) Cross-section TEM image of a Mg(4 nm)/Ti(2 nm) multilayer. The dashed rectangle highlights the presence of structural coherence at the interface between layers. Reprinted with permissions from [96] (copyright 2010 The American Physical Society). (**b**) Calculated structure of the $TiH_2(111)/MgH_2(101)$ interface (left) and of the $TiH_2(111)/Mg(0001)$ (right). Reprinted with permissions from [51] (copyright 2012 American Chemical Society).

Kalisvaart et al. suggested that it is possible to increase $\Delta\gamma^{int}$ up to 0.81 Jm^{-2} by replacing TiH_2 with TiAl, due to the stronger Al-Mg binding compared to Al-H [97]. They deposited Mg-AlTi multilayers with various combinations of layer thicknesses from Mg (20 nm)/AlTi (2 nm) to Mg (2 nm)/AlTi (2 nm). The total thickness of the multilayer stack was 500 nm so that it could be removed from the substrate and studied as a free standing sample, reaching a H storage capacity of 5.5 wt % [97]. It must be emphasized that a significant increase of the plateau pressure and hence a tangible destabilization emerge only for very thin Mg layers of 2–4 nm. In fact, Mg/Cr and Mg/V multilayers with a Mg thickness of about 18 nm did not show any significant thermodynamic alteration compared to bulk Mg [69], exhibiting $\Delta H^0 \approx 74$ kJ/molH_2 and $\Delta S^0 \approx 134$ J/K·molH_2 (see Table 1). Asano et al. showed that also MgH_2 clusters embedded within a TiH_2 film are destabilized because of interface energy effects [98].

A clarification on the different (de)stabilizing effects of enthalpy and entropy is necessary. In nanomaterials, the entropy associated with configurational disorder and vibrational dynamics within surface/interface regions brings a negative contribution $-Ts$ to the free energy, which counteracts the enthalpic destabilization. In the context of H sorption, the relevant question is the magnitude and sign of the entropy change Δs^{int} upon hydride formation. This topic has been far less explored by means of theoretical calculations than the enthalpy change Δh^{int}. In fact, $\Delta\gamma^{int}$ has been measured through model experiments, but it is Δh^{int} that has been calculated by theory, so that a direct determination of Δs^{int} is missing. The comparison between theory and experiments suggests that for Mg/MgH_2 within TiH_2 an entropy-driven stabilization significantly counteracts the impact of surface/interface enthalpy. In fact, calculations yield $\Delta h^{int}_{theo} \approx 0.64$ Jm^{-2} [51]. A rough estimation of the interfacial entropy change can be gained by combining experiment and theory into $\Delta s^{int} = (\Delta h^{int}_{theo} - \Delta\gamma^{\mathrm{int}})/T$, yielding $\Delta s^{int} \approx 1{\cdot}10^{-3}$ J/K·m^2. This discussion shows that further theoretical and experimental studies of interfacial entropy would help tailoring the thermodynamics of nanostructured hydrides by means of knowledge-based interface engineering.

5. Nano-Objects with a Composite Architecture

Recent advances in chemical synthesis and physical growth techniques have made it possible to design new materials with a composite morphology that combines different functionalities into a single nanoscale object ($L_{ext} << 100$ nm). This has often led to substantial improvement of H sorption behavior and deeper understanding of fundamental mechanisms, as highlighted by the examples below.

5.1. Core–Shell Nanoparticles

Zhang et al. developed a method to synthesize Mg_2NiH_4 NPs encapsulated in an MgO shell and supported on a graphene sheet via a gas–solid reaction method illustrated in Figure 9 [99]. In this method, Ni nanoparticles deposited on graphene by chemical reduction catalyze the formation of Mg_2Ni nanoparticles when exposed to Mg vapors. The Mg_2Ni intermetallic compound is one of the most studied materials for H storage. It offers better kinetic and thermodynamic properties compared to Mg at the expenses of a reduced storage capacity (~ 3.7 wt %). In the obtained nanostructure, Mg_2NiH_4 is the H-storage material, the MgO shell acts as confining medium, and graphene is an extremely light support that prevents interparticle coalescence during the synthesis.

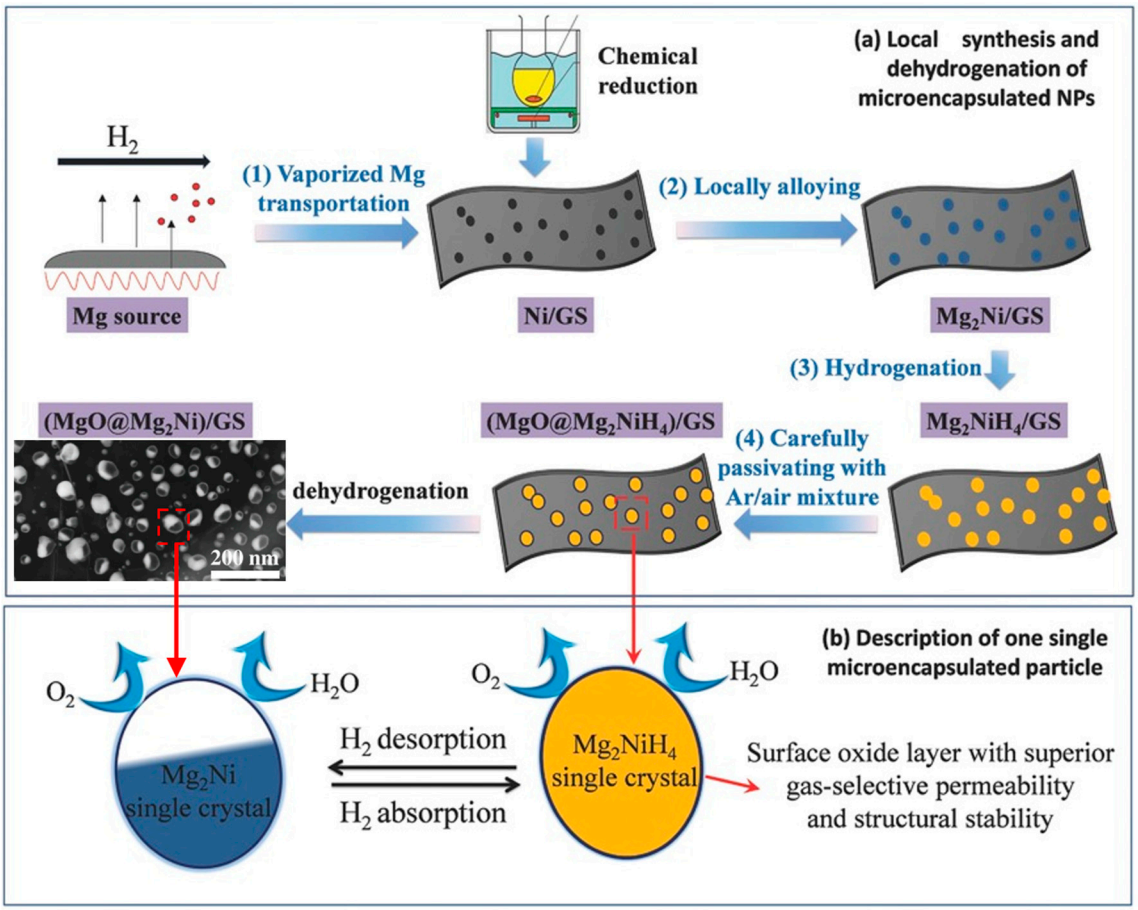

Figure 9. (**a**) Schematic of the local synthesis of Mg_2NiH_4 NPs derived from Ni/GS (graphene sheet) by hydriding chemical vapor deposition (HCVD). Mg vapors are transported under H_2 atmosphere to the Ni/GS substrate, where they alloy with Ni forming Mg_2Ni NPs. Subsequent hydrogenation and passivation lead to Mg_2NiH_4 NPs surrounded by an MgO shell. After H desorption, a semi-hollow core is left, as clearly shown by the scanning electron microscopy image in the bottom left corner. (**b**) The MgO shell is permeable to hydrogen but not to oxygen and water. Reprinted with permissions from [99] (copyright 2017 Wiley-VCH).

Interestingly, these NPs exhibit excellent H sorption kinetics and are not prone to further oxidation by residual oxygen and water impurities upon cycling. This result suggests that the thin (≈ 3 nm) MgO shell is permeable to H but not to oxygen and water, thus protecting the NPs. The reason for this behavior may be the easier diffusion of H across the MgO shell due to its small atomic size; however, further experiments and calculations are needed to elucidate the atomistic mechanisms behind the observed selectivity.

Moreover, the shell hampers inter-particle atomic diffusion and matter transport, preventing coarsening phenomena like Ostwald ripening and interparticle coalescence. A similar MgO-encapsulated morphology had also been realized in Mg NPs grown by gas-phase condensation [100,101], with one important difference. In the work of Zhang et al., the MgO shell is formed during the synthesis around the hydride core [99]. In this way, the shell never experiences strong mechanical stresses due to volume expansion. In fact, when the core transforms from Mg_2NiH_4 into Mg_2Ni upon H desorption, its volume contracts leaving a semi-hollow core as illustrated in Figure 9. This leaves room for volume expansion during the subsequent H absorption, when the original morphology is recovered without imposing a tensile stress on the shell. On the other hand, if the MgO shell were formed around the metallic core, the strong volume expansion that accompanies hydride formation could fracture the shell, leaving open channels for the evaporation of high vapor pressure elements (such as Mg) and leading to irreversible morphology changes [102].

These studies show that, at the nanoscale, a thin oxide layer is not necessarily detrimental to the H sorption properties. This appears in contrast to micron-sized powders or even larger samples, where surface oxidation may completely deactivate the material, as previously discussed for TiFe alloys. While a reason for this difference can be searched in the oxide thickness, another important point is the grain size of the oxide itself. In fact, an ultra-fine grain size of 3–4 nm is usually observed in MgO shells formed around Mg-based NPs [101]. The high fraction of GBs can therefore accelerate H diffusion in the direction perpendicular to the nanoparticle surface. Molecular dynamics simulations suggest that even Mg can diffuse sufficiently fast through MgO GBs at the typical temperatures adopted in H sorption experiments [103]. In conjunction with the tensile stresses imposed on the shell by volume expansion, this may induce irreversible morphological changes upon prolonged H cycling [102].

5.2. Thin Films Decorated with Nanoparticles

The relevance of fast diffusion pathways in allowing the penetration of H through surface oxides was recently highlighted by Kumar et al. using a surface-oxidized Mg films decorated with Pd NPs that act as H nanoportals [32]. DFT calculations and experimental observations of hydride domains (Figure 10) prove that H diffusion is prohibited at room temperature through a compact MgO layer and strongly inhibited through the hydride lattice.

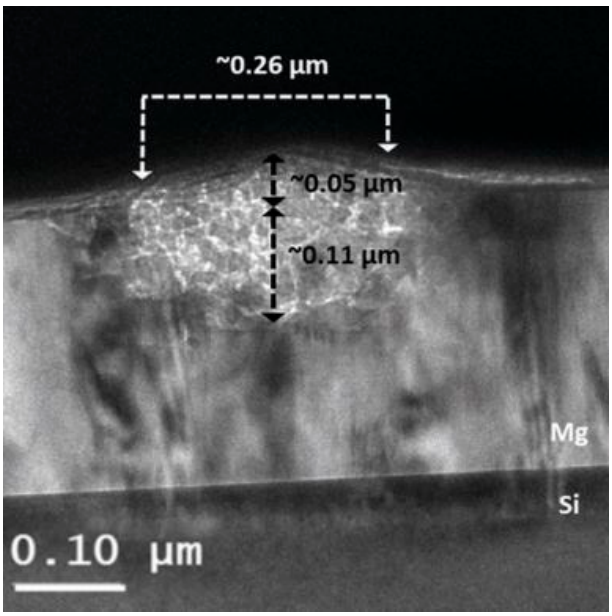

Figure 10. TEM observation of an MgH_2 nanodomain in an Mg film coated by a thin MgO layer. The domain, with depth ≈ 110 nm, lateral size ≈ 260 nm, and protrusion height ≈ 50 nm, forms below a Pd nanoparticle acting as a H nanoportal. Reprinted with permissions from [32] (copyright 2017 Wiley-VCH).

Moreover, coupling TEM observations with a diffusion model, the authors estimated a H diffusion coefficient through hydride domains $D_H \approx 8 \times 10^{-18}$ m^2 s^{-1}, in agreement with previous studies [45]. Remarkably, this value is about 7 orders of magnitude lower than H diffusion in metallic Mg, which is about 7×10^{-11} m^2 s^{-1} [45], as already mentioned in Section 2.1.

5.3. Composite Nanoparticles

The ultimate nanoscale system for H storage combines the hydride forming material with the catalyst in a single nano-object having a high surface-to-volume ratio. These architectures can achieve extremely fast kinetics along with thermodynamic changes. For instance, Patelli et al. have succeeded in assembling MgH_2-TiH_2 biphasic NPs by gas-phase condensation of mixed Mg-Ti vapors in a He-H_2 atmosphere, followed by hydrogenation at room temperature [24,33]. These composite NPs, shown in Figure 11a,b, can upload and release up to 4.8 wt % H_2, depending on the Mg/Ti ratio, in the remarkably low temperature range 100–150 °C without any precious metal catalysts (Figure 11d). The authors suggested that this is due to the combination of several factors: first of all, TiH_2 clusters facilitate the dissociation/recombination of the H_2 molecule; secondly, H atoms can diffuse rapidly along the Mg/TiH_2 interfaces, as discussed for Mg/TiH_2 films [104]; thirdly, internal interfaces act as favorable sites for heterogeneous nucleation; finally, the overall diffusion length is rather small corresponding to the nanoparticle size of 10–20 nm.

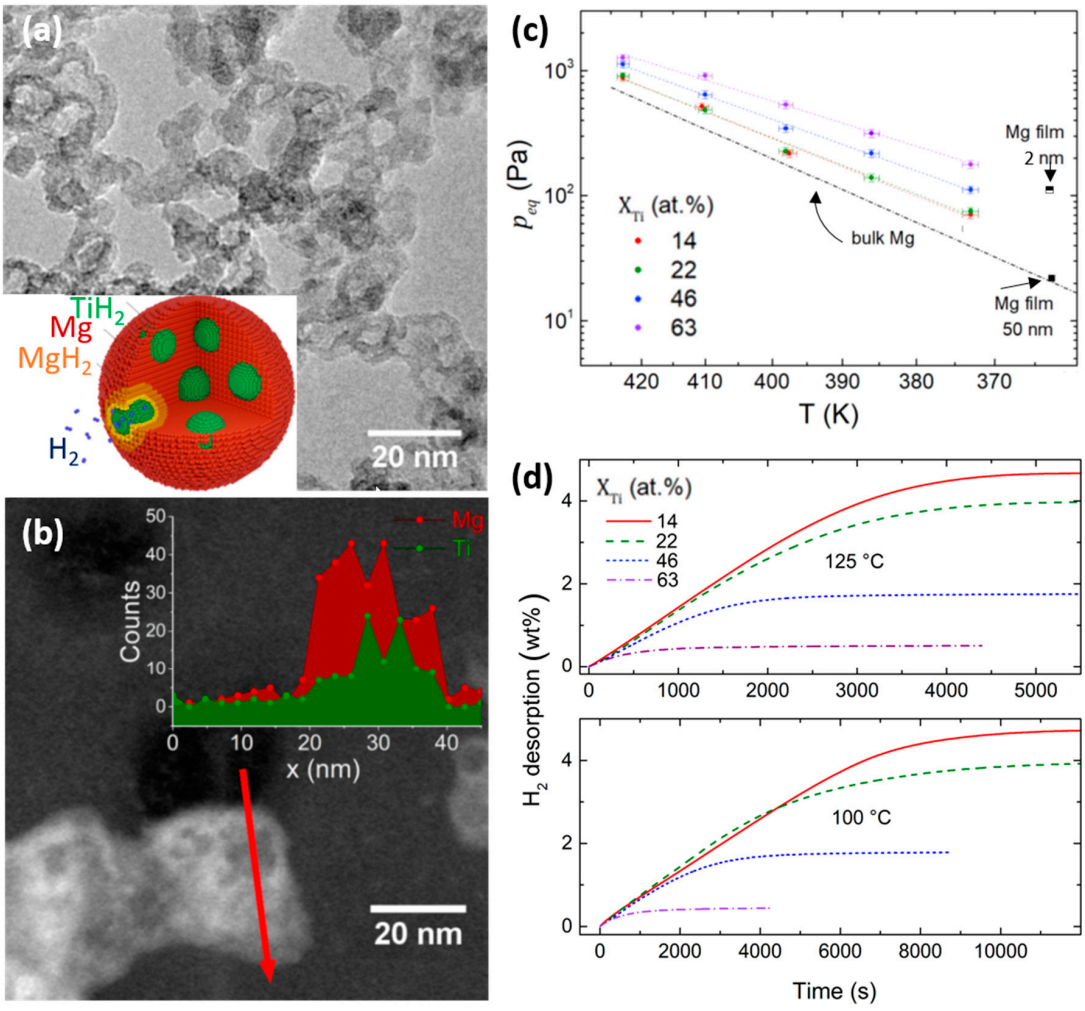

Figure 11. Morphology, composition and H sorption properties of MgH_2-TiH_2 biphasic NPs prepared by gas phase condensation of mixed Mg and Ti vapors. X_{Ti} represents the Ti/(Mg + Ti) atomic percentage.

(**a**) Bright field TEM image of NPs with $X_{Ti} = 14$; the inset depicts schematically the two-phase structure and the envisaged hydride formation mechanism. (**b**) High-angle annular dark field scanning TEM of one NP in (**a**); the inset shows the counts of Mg and Ti K-line x-rays scanned along the red arrow. (**c**) van 't Hoff plots for different X_{Ti} values; the line expected for bulk Mg and the data measured on Mg films of different thickness are shown for comparison. Reprinted with permissions from [24] (copyright 2020 Elsevier). (**d**) H_2 desorption kinetics from the same NPs at remarkably low temperature (100 and 125 °C). Reprinted with permissions from [33] (copyright 2019 Wiley-VCH).

The MgH_2-TiH_2 biphasic NPs also show a composition dependent thermodynamics, in which the two-phase plateau shifts slightly upward with increasing Ti content (Figure 11c). This behavior is ascribed to the free energy change $\Delta\gamma^{int}$ that occurs at internal interfaces upon MgH_2 formation/decomposition, as discussed in Section 2.2. A value $\Delta\gamma^{int} \approx 0.38$ J/m^2 was determined at T = 100 °C [24], in good agreement with the aforementioned studies of MgH_2/TiH_2 multilayers [23] and with DFT calculations [51]. The corresponding thermodynamical bias $\delta\Delta G^0$ spans the range 2–5 kJ/molH_2 depending on the diameter and volume fraction of the TiH_2 clusters.

Another interesting example of composite nano-objects is the synthesis of coated Mg NPs as small as 7 nm obtained by first reducing dibutylmagnesium ($MgBu_2$) with Li [105]. Subsequent coating with Co, Fe, Ni, Si, and Ti was obtained via transmetalation; the Mg NPs act as a reducing agent, at the surface of which the precursors are deposited directly. Upon hydriding at high temperature, the coating elements formed complex transition metal hydrides (Mg_2CoH_5, Mg_2FeH_6, and Mg_2NiH_4) or TiH_2. The authors highlighted a positive correlation between the desorption time and the reported activation energy for H desorption by the coating material. A modest decrease of the equilibrium plateau pressure compared to naked MgH_2 NPs was also reported, from a 5% for Ti and Si to a 15% reduction for Ni, which the authors correlated with the electronegativity of the coating element [105].

5.4. Nanoconfined Hydrides in Porous Scaffolds and Graphene-Based Materials

Numerous synthesis routes have been applied to stabilize small metal hydride NPs against sintering and surface contamination issues that occur on H cycling. A widely pursued strategy is the incorporation into a porous host that acts as scaffold and confining medium at the same time. The most popular host materials for this purpose are carbon-based scaffolds such as aerogels, high surface area graphite (HSAG), activated carbon, ordered mesoporous carbon (OMC), and carbon nanofibers. Mesoporous silica materials such as SBA-15 and MCM-41 that exhibit regular arrays of mesoporous channels have been explored, although their high density has a negative impact on the overall H storage capacity. Metal-organic frameworks (MOFs) are also being studied as promising scaffolds in this context, because they contain monodisperse micropores <2 nm. A survey of the most common host materials and their porous structure can be found in refs [39,106].

The synthesis routes for hydride nanoconfinement include solvent impregnation, melt infiltration, and synthesis inside the pores [39]. Solvent impregnation exploits the solubility of hydrides in solvents such as ethers or THF. The porous host is then soaked in the solution, a step that can be reiterated in order to enhance the loading of the hydride. Melt infiltration can be applied to hydrides with a low melting point; sometimes, eutectic mixtures are employed to lower the melting point and facilitate incorporation. A fine mixture of the hydride with the scaffold is heated in a furnace, very often under a H_2 backpressure to avoid desorption [40]. This approach can attain loadings up to 50–65% for MgH_2, $LiBH_4$, and $NaAlH_4$. Finally, the direct hydride synthesis inside the pores is usually carried out soaking the host material in a solution of $MgBu_2$. After removing the solvent, a hydrogenation step converts the $MgBu_2$ distributed within the pores into MgH_2 and butane gas [107]. Metal and hydride NPs confined in porous hosts can be refined to a diameter <5 nm [21,66,106,108,109]. In general, these composite architectures display excellent H sorption kinetics due to the ultra-small size L_{ext}. Moreover, they are quite stable on H cycling because the scaffold hinders NPs coalescence.

As an example, Figure 12a shows a distribution of Rh NPs synthesized by solvent impregnation on HSAG. The final loading was 10 wt % Rh over the total sample mass. These NPs exhibit hydride formation at mild H_2 pressure at room temperature. This is surprising because bulk Rh, due to the positive enthalpy of hydride formation $\Delta H^0 \approx 17$ kJ/mol H_2, transforms into hydride only under extremely high H_2 pressure (4 GPa). In striking contrast, the hydride phase forms below 0.1 MPa in ultra-fine Rh NPs, suggesting a nanoscale effect that drastically changes the Rh–H thermodynamics [110].

The major drawback of the supported NPs architecture is the weight ballast given by the scaffold material that implies a strong reduction of the H storage capacity. In order to overcome this issue, the strategy of embedding or wrapping the NPs using 2-D graphene-based sheets has recently emerged as a promising alternative. The key points of this idea are: (i) the sheets are atomically thin, so that the weight of the H-inactive material is at a minimum, and (ii) the NPs are protected from oxidation because H_2 is small and can diffuse through the sheets, whereas other molecules such as O_2 and H_2O cannot. As an example, MgH_2 NPs supported on graphene have been fabricated by the hydrogenation of $MgBu_2$ in cyclohexane under the structure-directing role of graphene [67]. This method gives a large number of monodisperse NPs with an average diameter of about 5.7 nm and free of agglomeration, as shown in Figure 12b. Additional doping with Ni leads to fast kinetics, reversible storage capacity of 5.5 wt %, and excellent stability under cycling (see also Table 1). Another example is the case of Mg_2NiH_4 NPs coated by MgO discussed in Section 5.1, which employed graphene sheets as substrate [99]. As a further case study, Cho et al. have demonstrated that reduced graphene oxide (rGO) sheets can be employed to embed Mg NPs protecting them from oxidation, thus allowing prolonged exposure to atmospheric conditions [66]. They achieved a remarkable 6.5 wt % H-storage capacity and low activation energy for H sorption, as listed in Table 1.

For all nanoconfined architectures, the main role of the supporting or embedding medium is physical confinement, which suppresses the growth of NPs improving their cycling stability. In addition, the arguments developed in Section 2.2 make it clear that elastic strains due to the confining host can alter the thermodynamics of hydride formation in the NPs, in a way similar to geometrical and microstructural constraints in thin films and core–shell NPs. In general, it is desirable that the support is inert and does not react with the NPs, but in reality, chemical interactions are not fully negligible. For instance, residual O in the C-based host may react with Mg decreasing the storage capacity over time. There are also tailored solutions, in which a catalytically active host assists H_2 dissociation and recombination, improving the kinetics. An interesting example is given by 3-D carbon coordinated with transition metals (Ni, Co, and Fe); MgH_2 NPs incorporated within this host by direct synthesis in the pores exhibit excellent air stability and H sorption kinetics [68]. Finally, it must be mentioned that the electronic coupling between the metallic NPs and graphene modifies the electronic properties of the latter. As concerns specifically the hydride, Berseth et al. have studied the interaction of $NaAlH_4$ with fullerenes, carbon nanotubes and graphene [111]. They showed that these materials catalyze H sorption in $NaAlH_4$ by reducing the ability of electron donation from Na to AlH_4. An extended discussion on electronic coupling and chemical interactions between NPs and host can be found in the review by Schneemann et al. [39].

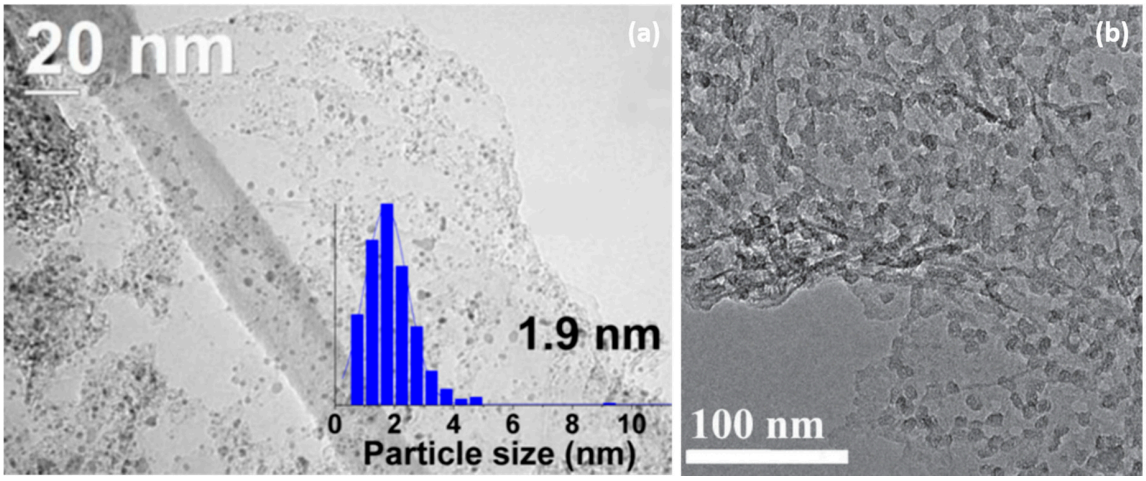

Figure 12. TEM images of nanoconfined NPs. (**a**) Rh NPs supported on HSAG prepared by impregnation with a $RhCl_3$ aqueous solution and subsequent reduction in Ar/H_2 at 200 °C. The inset shows the particle size histogram. Reprinted with permissions from [110] (copyright 2015 American Chemical Society). (**b**) MgH_2 NPs self-assembled on graphene, obtained by hydrogenation of adsorbed $MgBu_2$. Reprinted with permissions from [67] (copyright 2015 Wiley-VCH).

6. In Situ Observations of the Metal–Hydride Transformation

Recent progresses of in situ transmission electron microscopy (TEM) and spectroscopic methods have made it possible to characterize the H sorption properties of individual NPs. Langhammer and co-workers pioneered the use of indirect plasmonic sensing to measure hydride formation isotherms of single Pd and Mg NPs in contact with plasmonic Au nano-antennas [112]. This technique was applied to measure ΔH^0 and ΔS^0 in individual Pd NPs of different size (between 18 and 63 nm cube edge) and shape, showing that they are almost size- and shape-independent [35].

Individual Pd NPs undergo sharp transitions between the metal and hydride phases, as shown by in situ electron energy loss spectroscopy (EELS) in an environmental TEM (ETEM) [34]. The size dependence of the absorption plateau pressure can be explained by surface stress due to excess H concentration at the surface. The phase transformation appears as a coherent process with no phase coexistence, in agreement with the thermodynamic theory of Schwarz and Khachaturyan for open systems with coherent interfaces [113]. Again by a combination of EELS and scanning TEM (STEM), Narayan et al. captured the mechanism of nucleation and growth starting at the corners of single crystalline Pd nanocubes from 15 to 80 nm, an example of which is shown in Figure 13 [114]. In contrast to single crystal cubes and prisms, multiply twinned NPs absorb H gradually over several pressure steps and apparently exhibit reduced H storage capacity [115]. These fascinating single particle observations have been restricted to NPs $\gtrsim$ 15 nm due to experimental constraints. It will be interesting to see whether future experimental progress will allow investigating even smaller NPs.

Griessen et al. thoroughly examined experimental thermodynamic data for Pd NPs, showing that hydride formation is consistent with a coherent interface model and differs significantly from bulk Pd [30]. They developed a mean-field model, in which a H-rich surface shell imposes an elastic strain on the H-poor core. According to this model, H desorption is expected to proceed coherently only for small NPs (<50 nm); for large NPs the strain energy is relieved through nucleation of dislocations, and the transformation becomes partially incoherent as in bulk Pd.

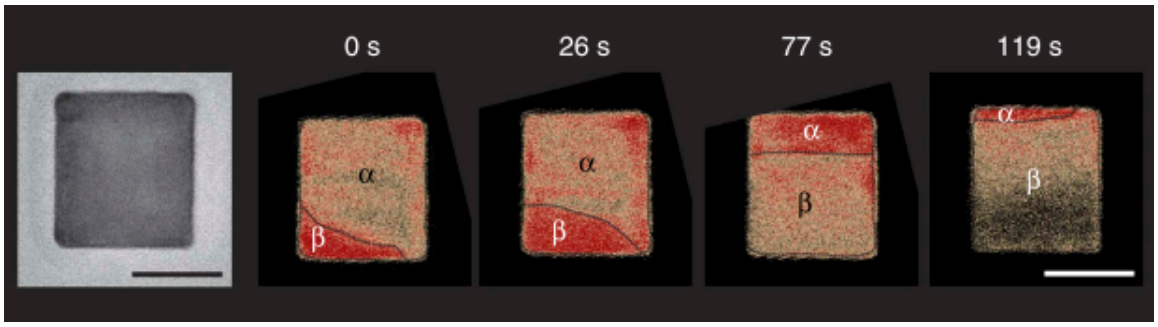

Figure 13. Still frames of the metal–hydride phase transformation in a 36 nm Pd nanocube as followed with STEM. The dotted lines represent the approximate locations of the phase boundaries (scale bar 25 nm). Reproduced with permission from [114] (copyright 2017 Springer Nature).

The role of dislocations in the phase transformation dynamics has been highlighted by Ulvestad et al. using Bragg coherent diffractive imaging (BCDI) to visualize the dislocation network evolution in single Pd NPs [36]. In BCDI, the 3-D strain and shape details are determined by acquiring coherent diffraction patterns of a single Bragg peak from an individual NP.

Using BCDI, the authors obtained 3-D images of the dislocation network at various times during exposure to a constant H_2 pressure. They found that even quite large particles ($270 \times 270 \times 135$ nm^3) persist in the α phase after a long exposure (390 min), with no indications that the transformation to the β phase has started. It seems that the transformation is hampered because the particles are too small to allow nucleation of dislocations, but too large to permit a coherent phase change. The critical size for dislocation nucleation is estimated as $\approx$ 300 nm, which is significantly larger than estimated by the aforementioned core–shell model [30,34]. A possible reason for this discrepancy may be the actual 3-D morphology of the particle and the magnitude of the associated strain energy. Indeed, BCDI reveals that the β phase resembles more a spherical cap on the α phase than an embedding shell around it. Using a 3-D phase field modeling, it can be calculated that this morphology lowers the strain energy by a factor of about 8, suppressing the driving force for dislocation nucleation [36]. It is also possible that the actual morphology of the NPs exposed to H depends on their shape, preparation method, and H_2 pressure. Therefore, a full assessment of the atomistic transformation mechanisms requires the use of complementary advanced techniques on the same samples.

We conclude this section highlighting an in situ TEM study of the metal–hydride transformation in the particularly challenging Mg-H system. The TEM observation of hydride formation in Mg is difficult due to its high reactivity and to the instability of MgH_2 under electron beam irradiation [116]. Despite these challenges, Hamm et al. have recently carried out successful in situ studies of MgH_2 precipitation and growth in a Mg film [117]. They used an ETEM combining EELS with various imaging techniques, and showed that the MgH_2 phase develops through the nucleation of nanograins separated by low-angle GBs. Mechanical stresses responsible for local plasticity and nanocrystallization have a marked influence on the phase transformation. Moreover, the increased stress state in Mg thin films destabilizes the hydride at ambient conditions. This study confirms the great potential of ETEM to unravel the mechanisms of solute-induced phase transformations.

7. Summary and Outlook

Several structural features of nanomaterials can be exploited to improve their H storage properties with respect to coarse-grained alloys. Besides the obvious kinetic advantage related to the nanoscale size and to the high surface-to-volume ratio, this review highlights the relevance of other phenomena that deserve deeper understanding by means of future experimental and theoretical work. For instance, the H-induced change of the specific free energy of surfaces, interfaces and grain boundaries shifts the equilibrium pressure compared to bulk systems, as experimentally shown in multilayers and composite nanoparticles. However, both the magnitude and the sign of this effect depend on atomistic

structural details that are known only for few materials; moreover, its separation into enthalpic and entropic contributions is far from being established. The presence of compressive elastic strains, of microstructural or geometrical origin, can induce a similar destabilization of the hydride phase. Nonetheless, the transition from the elastic to the plastic deformation regime must be controlled if strain engineered hydrides have to become a reality. The magnitude of the strain fields has an impact on the phase transformation mechanisms, being related to the critical size for dislocation nucleation in small particles. This aspect is important also for the application of nanoparticles in hydrogen sensors where a small pressure hysteresis and an excellent reproducibility are required. This discussion emphasizes the importance of knowledge-based materials design coupled with a careful assessment of the relations between microstructure, properties and mechanisms.

Recent advances in nanomaterials preparation methods have made it possible to realize nano-objects with composite architectures, in which different functionalities are combined at the nanoscale, e.g., catalysis, H storage, and protection from oxidation. This progress not only leads to materials with excellent H sorption properties, but also boosts the fundamental science of H in metals, unraveling transformation mechanisms at the nanoscale. The development of in situ microscopy and spectroscopy techniques is of paramount importance in this context and opens new exciting avenues for high-resolution experiments that reach out to other materials science branches.

Funding: This research received no external funding.

Acknowledgments: I would like to thank Ennio Bonetti for his inspiring views into the fascinating realm of materials microstructure down to the nanoscale.

Conflicts of Interest: The author declares no conflict of interest.

References

1. US DOE Hydrogen & Fuel Cells Program. Available online: https://www.hydrogen.energy.gov/ (accessed on 30 June 2020).
2. EERA-JP Fuel Cells and Hydrogen Implementation Plan. Available online: https://www.eera-set.eu/news-resources/78:eera-jp-fuel-cells-and-hydrogen-publishes-its-implementation-plan-up-to-2030.html (accessed on 30 June 2020).
3. van de Krol, R.; Grätzel, M. *Photoelectrochemical Hydrogen Production*; van de Krol, R., Grätzel, M., Eds.; Springer: Boston, MA, USA, 2012.
4. SUNERGY-Unlocking the Renewable Energy Future. Available online: https://www.sunergy-initiative.eu/ (accessed on 30 June 2020).
5. Carrette, L.; Friedrich, K.A.; Stimming, U. Fuel cells-fundamentals and applications. *Fuel Cells* **2001**, *1*, 5–39. [CrossRef]
6. Steele, B.C.H.; Heinzel, A. Materials for fuel-cell technologies. *Nature* **2001**, *414*, 345–352. [CrossRef] [PubMed]
7. Schlapbach, L.; Züttel, A. Hydrogen-storage materials for mobile applications. *Nature* **2001**, *414*, 353–358. [CrossRef] [PubMed]
8. Eberle, U.; Felderhoff, M.; Schüth, F. Chemical and physical solutions for hydrogen storage. *Angew. Chem. Int. Ed.* **2009**, *48*, 6608–6630. [CrossRef]
9. Møller, K.T.; Jensen, T.R.; Akiba, E.; Li, H. Hydrogen-A sustainable energy carrier. *Prog. Nat. Sci. Mater. Int.* **2017**, *27*, 34–40. [CrossRef]
10. Züttel, A. Materials for hydrogen storage. *Mater. Today* **2003**, *6*, 24–33. [CrossRef]
11. Hirscher, M.; Yartys, V.A.; Baricco, M.; Bellosta von Colbe, J.; Blanchard, D.; Bowman, R.C.; Broom, D.P.; Buckley, C.E.; Chang, F.; Chen, P.; et al. Materials for hydrogen-based energy storage—Past, recent progress and future outlook. *J. Alloy. Compd.* **2020**, *827*, 153548. [CrossRef]
12. Yartys, V.A.; Lototskyy, M.V.; Akiba, E.; Albert, R.; Antonov, V.E.; Ares, J.R.; Baricco, M.; Bourgeois, N.; Buckley, C.E.; Bellosta von Colbe, J.M.; et al. Magnesium based materials for hydrogen based energy storage: Past, present and future. *Int. J. Hydrogen Energy* **2019**, *44*, 7809–7859. [CrossRef]
13. Chen, P.; Zhu, M. Recent progress in hydrogen storage. *Mater. Today* **2008**, *11*, 36–43. [CrossRef]

14. Sandrock, G. Panoramic overview of hydrogen storage alloys from a gas reaction point of view. *J. Alloy. Compd.* **1999**, *293*, 877–888. [CrossRef]
15. US DOE Target Explanation Document: Onboard Hydrogen Storage for Light-Duty Fuel Cell Vehicles. Available online: www.energy.gov/eere/fuelcells/downloads/target-explanation-document-onboard-hydrogen-storage-light-duty-fuel-cell (accessed on 30 June 2020).
16. Callini, E.; Aguey-Zinsou, K.-F.; Ahuja, R.; Ares, J.R.; Bals, S.; Biliškov, N.; Chakraborty, S.; Charalambopoulou, G.; Chaudhary, A.-L.; Cuevas, F.; et al. Nanostructured materials for solid-state hydrogen storage: A review of the achievement of COST Action MP1103. *Int. J. Hydrogen Energy* **2016**, *41*, 14404–14428. [CrossRef]
17. Gleiter, H. Nanostructured materials: Basic concepts and microstructure. *Acta Mater.* **2000**, *48*, 1–29. [CrossRef]
18. Dosch, H. Some general aspects of confinement in nanomaterials. *Appl. Surf. Sci.* **2001**, *182*, 192–195. [CrossRef]
19. Pundt, A. Hydrogen in Nano-sized Metals. *Adv. Eng. Mater.* **2004**, *6*, 11–21. [CrossRef]
20. Bérubé, V.; Radtke, G.; Dresselhaus, M.; Chen, G. Size effects on the hydrogen storage properties of nanostructured metal hydrides: A review. *Int. J. Energy Res.* **2007**, *31*, 637–663. [CrossRef]
21. de Jongh, P.E.; Allendorf, M.; Vajo, J.J.; Zlotea, C. Nanoconfined light metal hydrides for reversible hydrogen storage. *MRS Bull.* **2013**, *38*, 488–494. [CrossRef]
22. Sachs, C.; Pundt, A.; Kirchheim, R.; Winter, M.; Reetz, M.; Fritsch, D. Solubility of hydrogen in single-sized palladium clusters. *Phys. Rev. B* **2001**, *64*, 075408. [CrossRef]
23. Mooij, L.P.A.; Baldi, A.; Boelsma, C.; Shen, K.; Wagemaker, M.; Pivak, Y.; Schreuders, H.; Griessen, R.; Dam, B. Interface energy controlled thermodynamics of nanoscale metal hydrides. *Adv. Energy Mater.* **2011**, *1*, 754–758. [CrossRef]
24. Patelli, N.; Migliori, A.; Morandi, V.; Pasquini, L. Interfaces within biphasic nanoparticles give a boost to magnesium-based hydrogen storage. *Nano Energy* **2020**, *72*, 104654. [CrossRef]
25. Barkhordarian, G.; Klassen, T.; Bormann, R. Catalytic mechanism of transition-metal compounds on Mg hydrogen sorption reaction. *J. Phys. Chem. B* **2006**, *110*, 11020–11024. [CrossRef]
26. Rizo-Acosta, P.; Cuevas, F.; Latroche, M. Hydrides of early transition metals as catalysts and grain growth inhibitors for enhanced reversible hydrogen storage in nanostructured magnesium. *J. Mater. Chem. A* **2019**, *7*, 23064. [CrossRef]
27. Baldi, A.; Gonzalez-Silveira, M.; Palmisano, V.; Dam, B.; Griessen, R. Destabilization of the Mg-H system through elastic constraints. *Phys. Rev. Lett.* **2009**, *102*, 1–4. [CrossRef]
28. Pasquini, L.; Sacchi, M.; Brighi, M.; Boelsma, C.; Bals, S.; Perkisas, T.; Dam, B. Hydride destabilization in core-shell nanoparticles. *Int. J. Hydrogen Energy* **2014**, *39*. [CrossRef]
29. Cornish-Bowden, A. Enthalpy-entropy compensation: A phantom phenomenon. *J. Biosci.* **2002**, *27*, 121–126. [CrossRef] [PubMed]
30. Griessen, R.; Strohfeldt, N.; Giessen, H. Thermodynamics of the hybrid interaction of hydrogen with palladium nanoparticles. *Nat. Mater.* **2016**, *15*, 311–317. [CrossRef]
31. Huot, J.; Ravnsbæk, D.B.; Zhang, J.; Cuevas, F.; Latroche, M.; Jensen, T.R. Mechanochemical synthesis of hydrogen storage materials. *Prog. Mater. Sci.* **2013**, *58*, 30–75. [CrossRef]
32. Kumar, S.; Pavloudis, T.; Singh, V.; Nguyen, H.; Steinhauer, S.; Pursell, C.; Clemens, B.; Kioseoglou, J.; Grammatikopoulos, P.; Sowwan, M. Hydrogen Flux through Size Selected Pd Nanoparticles into Underlying Mg Nanofilms. *Adv. Energy Mater.* **2018**, *8*, 1701326. [CrossRef]
33. Patelli, N.; Migliori, A.; Pasquini, L. Reversible metal-hydride transformation in Mg-Ti-H nanoparticles at remarkably low temperatures. *Chem. Phys. Chem.* **2019**, *20*, 1325–1333. [CrossRef]
34. Baldi, A.; Narayan, T.C.; Koh, A.L.; Dionne, J. A in situ detection of hydrogen-induced phase transitions in individual palladium nanocrystals. *Nat. Mater.* **2014**, *13*. [CrossRef]
35. Syrenova, S.; Wadell, C.; Nugroho, F.A.A.; Gschneidtner, T.A.; Diaz Fernandez, Y.A.; Nalin, G.; Świtlik, D.; Westerlund, F.; Antosiewicz, T.J.; Zhdanov, V.P.; et al. Hydride formation thermodynamics and hysteresis in individual Pd nanocrystals with different size and shape. *Nat. Mater.* **2015**, *14*, 1236–1244. [CrossRef]
36. Ulvestad, A.; Welland, M.J.; Cha, W.; Liu, Y.; Kim, J.W.; Harder, R.; Maxey, E.; Clark, J.N.; Highland, M.J.; You, H.; et al. Three-dimensional imaging of dislocation dynamics during the hydriding phase transformation. *Nat. Mater.* **2017**, *16*, 565–571. [CrossRef] [PubMed]

37. Pundt, A.; Kirchheim, R. Hydrogen in metals: Microstructural Aspects. *Annu. Rev. Mater. Res.* **2006**, *36*, 555–608. [CrossRef]
38. Pasquini, L. The effects of nanostructure on the hydrogen sorption properties of magnesium-based metallic compounds: A review. *Crystals* **2018**, *8*, 106. [CrossRef]
39. Schneemann, A.; White, J.L.; Kang, S.; Jeong, S.; Wan, L.F.; Cho, E.S.; Heo, T.W.; Prendergast, D.; Urban, J.J.; Wood, B.C.; et al. Nanostructured metal hydrides for hydrogen Storage. *Chem. Rev.* **2018**, *118*, 10775–10839. [CrossRef]
40. De Jongh, P.E.; Adelhelm, P. Nanosizing and nanoconfinement: New strategies towards meeting hydrogen storage goals. *ChemSusChem* **2010**, *3*, 1332–1348. [CrossRef]
41. Zou, J.; Sun, H.; Zeng, X.; Ji, G.; Ding, W. Preparation and hydrogen storage properties of MG-rich Mg-Ni ultrafine particles. *J. Nanomater.* **2012**, *2012*, 1–8. [CrossRef]
42. Schwarz, R.B.; Khachaturyan, A.G. Thermodynamics of open two-phase systems with coherent interfaces: Application to metal-hydrogen systems. *Acta Mater.* **2006**, *54*, 313–323. [CrossRef]
43. Mooij, L.; Dam, B. Hysteresis and the role of nucleation and growth in the hydrogenation of Mg nanolayers. *Phys. Chem. Chem. Phys.* **2013**, *15*, 2782–2792. [CrossRef]
44. Fukai, Y. *The Metal-Hydrogen System: Basic Bulk Properties*; Springer: Berlin/Heidelberg, Germany, 2005.
45. Uchida, H.T.; Wagner, S.; Hamm, M.; Kürschner, J.; Kirchheim, R.; Hjörvarsson, B.; Pundt, A. Absorption kinetics and hydride formation in magnesium films: Effect of driving force revisited. *Acta Mater.* **2015**, *85*, 279–289. [CrossRef]
46. Mintz, M.H.; Zeiri, Y. Hydriding kinetics of powders. *J. Alloys Compd.* **1995**, *216*, 159–175. [CrossRef]
47. Borgschulte, A.; Gremaud, R.; Griessen, R. Interplay of diffusion and dissociation mechanisms during hydrogen absorption in metals. *Phys. Rev. B-Condens. Matter Mater. Phys.* **2008**, *78*, 1–16. [CrossRef]
48. Rudman, P.S. Hydrogen-diffusion-rate-limited hydriding and dehydring kinetics. *J. Appl. Phys.* **1979**, *50*, 7195–7199. [CrossRef]
49. Ron, M. The normalized pressure dependence method for the evaluation of kinetic rates of metal hydride formation/decomposition. *J. Alloys Compd.* **1999**, *283*, 178–191. [CrossRef]
50. Berube, V.; Chen, G.; Dresselhaus, M.S. Impact of nanostructuring on the enthalpy of formation of metal hydrides. *Int. J. Hydrogen Energy* **2008**, *33*, 4122–4131. [CrossRef]
51. Hao, S.Q.; Sholl, D.S. Effect of TiH2-induced strain on thermodynamics of hydrogen release from MgH2. *J. Phys. Chem. C* **2012**, *116*, 2045–2050. [CrossRef]
52. Molinari, A.; D'Amico, F.; Calizzi, M.; Zheng, Y.; Boelsma, C.; Mooij, L.; Lei, Y.; Hahn, H.; Dam, B.; Pasquini, L. Interface and strain effects on the H-sorption thermodynamics of size-selected Mg nanodots. *Int. J. Hydrogen Energy* **2016**, *41*, 9841–9851. [CrossRef]
53. Sun, Y.; Shen, C.; Lai, Q.; Liu, W.; Wang, D.-W.; Aguey-Zinsou, K.-F. Tailoring magnesium based materials for hydrogen storage through synthesis: Current state of the art. *Energy Storage Mater.* **2018**, *10*, 168–198. [CrossRef]
54. Asano, K.; Enoki, H.; Akiba, E. Synthesis of HCP, FCC and BCC structure alloys in the Mg-Ti binary system by means of ball milling. *J. Alloys Compd.* **2009**, *480*, 558–563. [CrossRef]
55. Zaluska, A.; Zaluski, L.; Ström-Olsen, J.O. Structure, catalysis and atomic reactions on the nano-scale: A systematic approach to metal hydrides for hydrogen storage. *Appl. Phys. A Mater. Sci. Process.* **2001**, *72*, 157–165. [CrossRef]
56. Barkhordarian, G.; Klassen, T.; Bormann, R. Kinetic investigation of the effect of milling time on the hydrogen sorption reaction of magnesium catalyzed with different Nb2O 5 contents. *J. Alloys Compd.* **2006**, *407*, 249–255. [CrossRef]
57. Lu, J.; Choi, Y.J.; Fang, Z.Z.; Sohn, H.Y.; Rönnebro, E. Hydrogen storage properties of nanosized MgH2-0.1TiH2 prepared by ultrahigh-energy-high-pressure milling. *J. Am. Chem. Soc.* **2009**, *131*, 15843–15852. [CrossRef] [PubMed]
58. Ravnsbœk, D.; Filinchuk, Y.; Cerenius, Y.; Jakobsen, H.J.; Besenbacher, F.; Skibsted, J.; Jensen, T.R. A series of mixed-metal borohydrides. *Angew. Chem. Int. Ed.* **2009**, *48*, 6659–6663. [CrossRef]
59. Huot, J.; Cuevas, F.; Deledda, S.; Edalati, K.; Filinchuk, Y.; Grosdidier, T.; Hauback, B.C.; Heere, M.; Jensen, T.R.; Latroche, M.; et al. Mechanochemistry of metal hydrides: Recent advances. *Materials* **2019**, *12*, 2778. [CrossRef] [PubMed]

60. Webb, C.J. A review of catalyst-enhanced magnesium hydride as a hydrogen storage material. *J. Phys. Chem. Solids* **2015**, *84*. [CrossRef]
61. Valiev, R.Z.; Islamgaliev, R.K.; Alexandrov, I.V. Bulk nanostructured materials from severe plastic deformation. *Prog. Mater. Sci.* **2000**, *45*, 103–189. [CrossRef]
62. Fernández, J.F.; Sánchez, C.R. Rate determining step in the absorption and desorption of hydrogen by magnesium. *J. Alloys Compd.* **2002**, *340*, 189–198. [CrossRef]
63. Paskevicius, M.; Sheppard, D.A.; Buckley, C.E. Thermodynamic changes in mechanochemically synthesized magnesium hydride nanoparticles. *J. Am. Chem. Soc.* **2010**, *6*, 469–472. [CrossRef]
64. Norberg, N.S.; Arthur, T.S.; Fredrick, S.J.; Prieto, A.L. Size-dependent hydrogen storage properties of Mg nanocrystals prepared from solution. *J. Am. Chem. Soc.* **2011**, *133*, 10679–10681. [CrossRef]
65. Li, W.; Li, C.; Ma, H.; Chen, J. Magnesium nanowires: Enhanced kinetics for hydrogen absorption and desorption. *J. Am. Chem. Soc.* **2007**, *129*, 6710–6711. [CrossRef]
66. Cho, E.S.; Ruminski, A.M.; Aloni, S.; Liu, Y.-S.; Guo, J.; Urban, J.J. Graphene oxide/metal nanocrystal multilaminates as the atomic limit for safe and selective hydrogen storage. *Nat. Commun.* **2016**, *7*, 10804. [CrossRef]
67. Xia, G.; Tan, Y.; Chen, X.; Sun, D.; Guo, Z.; Liu, H.; Ouyang, L.; Zhu, M.; Yu, X. Monodisperse magnesium hydride nanoparticles uniformly self-assembled on graphene. *Adv. Mater.* **2015**, *27*, 5981–5988. [CrossRef] [PubMed]
68. Shinde, S.S.; Kim, D.H.; Yu, J.Y.; Lee, J.H. Self-assembled air-stable magnesium hydride embedded in 3-D activated carbon for reversible hydrogen storage. *Nanoscale* **2017**, *9*, 7094–7103. [CrossRef] [PubMed]
69. Fry, C.M.P.; Grant, D.M.; Walker, G.S. Catalysis and evolution on cycling of nano-structured magnesium multilayer thin films. *Int. J. Hydrogen Energy* **2014**, *39*, 1173–1184. [CrossRef]
70. Cui, J.; Wang, H.; Liu, J.; Ouyang, L.; Zhang, Q.; Sun, D.; Yao, X.; Zhu, M. Remarkable enhancement in dehydrogenation of MgH2 by a nano-coating of multi-valence Ti-based catalysts. *J. Mater. Chem. A* **2013**, *1*, 5603. [CrossRef]
71. Liu, J.W.; Zou, C.C.; Wang, H.; Ouyang, L.Z.; Zhu, M. Facilitating de/hydrogenation by long-period stacking ordered structure in Mg based alloys. *Int. J. Hydrogen Energy* **2013**, *38*, 10438–10445. [CrossRef]
72. Yamauchi, M.; Ikeda, R.; Kitagawa, H.; Takata, M. Nanosize effects on hydrogen storage in palladium. *J. Phys. Chem. C* **2008**, *112*, 3294–3299. [CrossRef]
73. Bardhan, R.; Hedges, L.O.; Pint, C.L.; Javey, A.; Whitelam, S.; Urban, J.J. Uncovering the intrinsic size dependence of hydriding phase transformations in nanocrystals. *Nat. Mater.* **2013**, *12*. [CrossRef]
74. Edalati, K.; Matsuda, J.; Iwaoka, H.; Toh, S.; Akiba, E.; Horita, Z. High-pressure torsion of TiFe intermetallics for activation of hydrogen storage at room temperature with heterogeneous nanostructure. *Int. J. Hydrogen Energy* **2013**, *38*, 4622–4627. [CrossRef]
75. Révész, Á.; Gajdics, M.; Schafler, E.; Calizzi, M.; Pasquini, L. Dehydrogenation-hydrogenation characteristics of nanocrystalline Mg2Ni powders compacted by high-pressure torsion. *J. Alloys Compd.* **2017**, *702*, 84–91. [CrossRef]
76. Edalati, K.; Shao, H.; Emami, H.; Iwaoka, H.; Akiba, E.; Horita, Z. Activation of titanium-vanadium alloy for hydrogen storage by introduction of nanograins and edge dislocations using high-pressure torsion. *Int. J. Hydrogen Energy* **2016**, *41*, 8917–8924. [CrossRef]
77. Huot, J. Nanocrystalline metal hydrides obtained by severe plastic deformations. *Metals (Basel)* **2012**, *2*, 22–40. [CrossRef]
78. Révész, A.; Kánya, Z.; Verebélyi, T.; Szabó, P.J.; Zhilyaev, A.P.; Spassov, T. The effect of high-pressure torsion on the microstructure and hydrogen absorption kinetics of ball-milled Mg70Ni30. *J. Alloys Compd.* **2010**, *504*, 83–88. [CrossRef]
79. Gajdics, M.; Calizzi, M.; Pasquini, L.; Schafler, E.; Révész, A. Characterization of a nanocrystalline Mg-Ni alloy processed by high-pressure torsion during hydrogenation and dehydrogenation. *Int. J. Hydrogen Energy* **2016**, *41*, 9803–9809. [CrossRef]
80. Emami, H.; Edalati, K.; Matsuda, J.; Akiba, E.; Horita, Z. Hydrogen storage performance of TiFe after processing by ball milling. *Acta Mater.* **2015**, *88*, 190–195. [CrossRef]
81. Hongo, T.; Edalati, K.; Arita, M.; Matsuda, J.; Akiba, E.; Horita, Z. Significance of grain boundaries and stacking faults on hydrogen storage properties of Mg2Ni intermetallics processed by high-pressure torsion. *Acta Mater.* **2015**, *92*, 46–54. [CrossRef]

82. Edalati, K.; Akiba, E.; Horita, Z. High-pressure torsion for new hydrogen storage materials. *Sci. Technol. Adv. Mater.* **2018**, *19*, 185–193. [CrossRef] [PubMed]
83. Edalati, K.; Matsuda, J.; Arita, M.; Daio, T.; Akiba, E.; Horita, Z. Mechanism of activation of TiFe intermetallics for hydrogen storage by severe plastic deformation using high-pressure torsion. *Appl. Phys. Lett.* **2013**, *103*, 143902. [CrossRef]
84. Okuda, H.; Yamasaki, M.; Kawamura, Y.; Tabuchi, M.; Kimizuka, H. Nanoclusters first: A hierarchical phase transformation in a novel Mg alloy. *Sci. Rep.* **2015**, *5*, 1–6. [CrossRef]
85. Abe, E.; Kawamura, Y.; Hayashi, K.; Inoue, A. Long-period ordered structure in a high-strength nanocrystalline Mg-1 at% Zn-2 at% Y alloy studied by atomic-resolution Z-contrast STEM. *Acta Mater.* **2002**, *50*, 3845–3857. [CrossRef]
86. Itoi, T.; Seimiya, T.; Kawamura, Y.; Hirohashi, M. Long period stacking structures observed in Mg97Zn 1Y2 alloy. *Scr. Mater.* **2004**, *51*, 107–111. [CrossRef]
87. Zhang, Q.A.; Liu, D.D.; Wang, Q.Q.; Fang, F.; Sun, D.L.; Ouyang, L.Z.; Zhu, M. Superior hydrogen storage kinetics of Mg12YNi alloy with a long-period stacking ordered phase. *Scr. Mater.* **2011**, *65*, 233–236. [CrossRef]
88. Cermak, J.; Kral, L.; Roupcova, P. Significantly decreased stability of MgH2 in the Mg-In-C alloy system: Long-period-stacking-ordering as a new way how to improve performance of hydrogen storage alloys? *Renew. Energy* **2020**, *150*, 204–212. [CrossRef]
89. Yoshimura, K.; Langhammer, C.; Dam, B. Metal hydrides for smart window and sensor applications. *MRS Bull.* **2013**, *38*, 495–503. [CrossRef]
90. Nugroho, F.A.A.; Darmadi, I.; Cusinato, L.; Susarrey-Arce, A.; Schreuders, H.; Bannenberg, L.J.; da Silva Fanta, A.B.; Kadkhodazadeh, S.; Wagner, J.B.; Antosiewicz, T.J.; et al. Metal–polymer hybrid nanomaterials for plasmonic ultrafast hydrogen detection. *Nat. Mater.* **2019**, *18*, 489–495. [CrossRef] [PubMed]
91. Wagner, S.; Pundt, A. Quasi-thermodynamic model on hydride formation in palladium–hydrogen thin films: Impact of elastic and microstructural constraints. *Int. J. Hydrogen Energy* **2016**, *41*, 2727–2738. [CrossRef]
92. Chung, C.J.; Lee, S.C.; Groves, J.R.; Brower, E.N.; Sinclair, R.; Clemens, B.M. Interfacial alloy hydride destabilization in Mg/Pd thin films. *Phys. Rev. Lett.* **2012**, *108*, 1–4. [CrossRef]
93. Baldi, A.; Mooij, L.; Palmisano, V.; Schreuders, H.; Krishnan, G.; Kooi, B.J.; Dam, B.; Griessen, R. Elastic versus Alloying effects in Mg-based hydride films. *Phys. Rev. Lett.* **2018**, *121*, 255503. [CrossRef]
94. Pivak, Y.; Schreuders, H.; Dam, B. Thermodynamic properties, hysteresis behavior and stress-strain analysis of MgH2 thin films, studied over a wide temperature range. *Crystals* **2012**, *2*, 710–729. [CrossRef]
95. Ngene, P.; Longo, A.; Mooij, L.; Bras, W.; Dam, B. Metal-hydrogen systems with an exceptionally large and tunable thermodynamic destabilization. *Nat. Commun.* **2017**, *8*, 1846. [CrossRef]
96. Baldi, A.; Pálsson, G.K.; Gonzalez-Silveira, M.; Schreuders, H.; Slaman, M.; Rector, J.H.; Krishnan, G.; Kooi, B.J.; Walker, G.S.; Fay, M.W.; et al. Mg/Ti multilayers: Structural and hydrogen absorption properties. *Phys. Rev. B-Condens. Matter Mater. Phys.* **2010**, *81*, 1–10. [CrossRef]
97. Kalisvaart, P.; Shalchi-Amirkhiz, B.; Zahiri, R.; Zahiri, B.; Tan, X.; Danaie, M.; Botton, G.; Mitlin, D. Thermodynamically destabilized hydride formation in "bulk" Mg–AlTi multilayers for hydrogen storage. *Phys. Chem. Chem. Phys.* **2013**, *15*, 16432–16436. [CrossRef]
98. Asano, K.; Westerwaal, R.J.; Anastasopol, A.; Mooij, L.P.A.; Boelsma, C.; Ngene, P.; Schreuders, H.; Eijt, S.W.H.; Dam, B. Destabilization of Mg hydride by self-organized nanoclusters in the immiscible Mg–Ti system. *J. Phys. Chem. C* **2015**, *119*, 12157–12164. [CrossRef]
99. Zhang, J.; Zhu, Y.; Lin, H.; Liu, Y.; Zhang, Y.; Li, S.; Ma, Z.; Li, L. Metal hydride nanoparticles with ultrahigh structural stability and hydrogen storage activity derived from microencapsulated nanoconfinement. *Adv. Mater.* **2017**, *29*, 1700760. [CrossRef] [PubMed]
100. Pasquini, L.; Callini, E.; Piscopiello, E.; Montone, A.; Antisari, M.V.; Bonetti, E. Metal-hydride transformation kinetics in Mg nanoparticles. *Appl. Phys. Lett.* **2009**, *94*, 041918. [CrossRef]
101. Callini, E.; Pasquini, L.; Piscopiello, E.; Montone, A.; Antisari, M.V.; Bonetti, E. Hydrogen sorption in Pd-decorated Mg-MgO core-shell nanoparticles. *Appl. Phys. Lett.* **2009**, *94*, 221905. [CrossRef]
102. Pasquini, L.; Montone, A.; Callini, E.; Antisari, M.V.; Bonetti, E. Formation of hollow structures through diffusive phase transition across a membrane. *Appl. Phys. Lett.* **2011**, *99*, 021911. [CrossRef]
103. Landuzzi, F.; Pasquini, L.; Giusepponi, S.; Celino, M.; Montone, A.; Palla, P.L.; Cleri, F. Molecular dynamics of ionic self-diffusion at an MgO grain boundary. *J. Mater. Sci.* **2015**, *50*, 2502–2509. [CrossRef]

104. Duan, X.; Griessen, R.; Wijngaarden, R.J.; Kamin, S.; Liu, N. Self-recording and manipulation of fast long-range hydrogen diffusion in quasifree magnesium. *Phys. Rev. Mater.* **2018**, *2*, 085802. [CrossRef]
105. Liu, W.; Setijadi, E.J.; Aguey-Zinsou, K.-F. Tuning the thermodynamic properties of MgH2 at the nanoscale via a catalyst or destabilizing element coating strategy. *J. Phys. Chem. C* **2014**, *118*, 27781–27792. [CrossRef]
106. Nielsen, T.K.; Besenbacher, F.; Jensen, T.R. Nanoconfined hydrides for energy storage. *Nanoscale* **2011**, *3*, 2086–2098. [CrossRef] [PubMed]
107. Nielsen, T.K.; Manickam, K.; Hirscher, M.; Besenbacher, F.; Jensen, T.R. Confinement of MgH2 Nanoclusters within nanoporous aerogel scaffold materials. *ACS Nano* **2009**, *3*, 3521–3528. [CrossRef] [PubMed]
108. Zlotea, C.; Oumellal, Y.; Hwang, S.-J.; Ghimbeu, C.M.; de Jongh, P.E.; Latroche, M. Ultrasmall MgH2 nanoparticles embedded in an ordered microporous carbon exhibiting rapid hydrogen Sorption Kinetics. *J. Phys. Chem. C* **2015**, *119*, 18091–18098. [CrossRef]
109. Jeon, K.-J.; Moon, H.R.; Ruminski, A.M.; Jiang, B.; Kisielowski, C.; Bardhan, R.; Urban, J.J. Air-stable magnesium nanocomposites provide rapid and high-capacity hydrogen storage without using heavy-metal catalysts. *Nat. Mater.* **2011**, *10*, 286–290. [CrossRef] [PubMed]
110. Zlotea, C.; Oumellal, Y.; Msakni, M.; Bourgon, J.; Bastide, S.; Cachet-Vivier, C.; Latroche, M. First evidence of rh nano-hydride formation at low pressure. *Nano Lett.* **2015**, *15*, 4752–4757. [CrossRef] [PubMed]
111. Berseth, P.A.; Harter, A.G.; Zidan, R.; Blomqvist, A.; Araújo, C.M.; Scheicher, R.H.; Ahuja, R.; Jena, P. Carbon nanomaterials as catalysts for hydrogen uptake and release in NaAIH 4. *Nano Lett.* **2009**, *9*, 1501–1505. [CrossRef]
112. Shegai, T.; Langhammer, C. Hydride formation in single palladium and magnesium nanoparticles studied by nanoplasmonic dark-field scattering spectroscopy. *Adv. Mater.* **2011**, *23*, 4409–4414. [CrossRef]
113. Schwarz, R.B.; Khachaturyan, A.G. Thermodynamics of open two-phase systems with coherent interfaces. *Phys. Rev. Lett.* **1995**, *74*, 2523–2526. [CrossRef]
114. Narayan, T.C.; Hayee, F.; Baldi, A.; Koh, A.L.; Sinclair, R.; Dionne, J.A. Direct visualization of hydrogen absorption dynamics in individual palladium nanoparticles. *Nat. Commun.* **2017**, *8*, 14020. [CrossRef]
115. Narayan, T.C.; Baldi, A.; Koh, A.L.; Sinclair, R.; Dionne, J.A. Reconstructing solute-induced phase transformations within individual nanocrystals. *Nat. Mater.* **2016**, *15*, 768–774. [CrossRef]
116. Surrey, A.; Nielsch, K.; Rellinghaus, B. Comments on "Evidence of the hydrogen release mechanism in bulk MgH2". *Sci. Rep.* **2017**, *7*, 44216. [CrossRef]
117. Hamm, M.; Bongers, M.D.; Roddatis, V.; Dietrich, S.; Lang, K.H.; Pundt, A. In situ observation of hydride nucleation and selective growth in magnesium thin-films with environmental transmission electron microscopy. *Int. J. Hydrogen Energy* **2019**, *44*, 32112–32123. [CrossRef]